

Senescent Mesenchymal Stem Cells Remodel Extracellular Matrix Driving Breast Cancer Cells to More Invasive Phenotype

Deepraj Ghosh¹, Carolina Mejia-Pena², Nhat Quach¹, Botai Xuan¹, Amy H. Lee³, Michelle R. Dawson^{1,2,3*}

¹Brown University, Department of Molecular Pharmacology, Physiology, and Biotechnology, Providence, 02912, USA

²Brown University, Department of Molecular Biology, Cell Biology and Biochemistry, Providence, 02912, USA

³Brown University, Center for Biomedical Engineering, Providence, 02912, USA

*Correspondence addressed to michelle_dawson@brown.edu

Summary

Senescence-induced biophysical changes in mesenchymal stem cells enabled them to develop a matrix remodeling phenotype, which promoted increased cancer cell proliferation and invasion.

Abstract

Mesenchymal stem cells accumulated in tissue specific sites are essential for the regenerative process; however, biological aging and environmental stress can induce senescence - an irreversible state of growth arrest - that not only affects the behavior of cells but also disrupts their ability to restore tissue integrity. While abnormal tissue properties including increased extracellular matrix stiffness are linked with the risk of developing breast cancer, the role and contribution of senescent MSCs to the disease progression to malignancy are not well understood. Here, we investigated senescence associated biophysical changes in MSCs and how they influence cancer cell behavior in a 3D matrix interface model. Although senescent MSCs were far less motile than pre-senescent MSCs, they induced an invasive breast cancer phenotype, characterized by increased spheroid growth and cell invasion in collagen gels. Further analysis of collagen gels using second harmonic generation showed increased collagen density when senescent MSCs were present, suggesting that senescent MSCs actively remodel the surrounding matrix. This study provides direct evidence of the pro-malignant effects of senescent MSCs in tumors.

Introduction

Mesenchymal stem cells (MSCs) are multipotent progenitor cells that reside in bone marrow and connective tissues and differentiate into multiple cell types required for normal tissue maintenance and repair. Homing of MSCs to tumors has been documented in multiple cancer types, including breast(Studený *et al.*, 2002), colon(O'Malley *et al.*, 2016), and ovarian carcinomas(McLean *et al.*, 2011) and gliomas(Ho *et al.*, 2013). MSCs modulate the behavior of other cells by secreting signaling molecules, matrix proteins, or enzymes to alter their function(Caplan and Dennis, 2006). These MSC-secreted factors can modulate tumor bystander effects after radiotherapy(Farias *et al.*, 2015), suppress the immune response to tumors(Uccelli, Moretta and Pistoia, 2008), and drive the formation of more invasive cancer cell phenotypes(Karnoub *et al.*, 2007; McAndrews, McGrail, *et al.*, 2015). MSCs also differentiate into carcinoma associated fibroblasts (CAFs) that play a central role in tumor growth and matrix remodeling by increasing matrix deposition, cross-linking, and bundling for increased tissue stiffness(Orimo *et al.*, 2005; Kalluri and Zeisberg, 2006), activating mechanosensitive signaling pathways(Kümper and Marshall, 2011), and generating force and protease-mediated tracks that cancer cells can follow during metastasis(Carey, Martin and Reinhart-King, 2017). MSCs are highly resistant to apoptosis(Vallabhaneni *et al.*, 2016) but undergo senescence in response to DNA damage, replicative stress, or genotoxic stress from environmental toxins, therapeutic agents, or ionizing radiation(Kasper *et al.*, 2009; Wagner *et al.*, 2009; Alessio *et al.*, 2015). Growth is irreversibly arrested in senescent cells; however, they remain metabolically active and develop a senescence associated secretory phenotype (SASP)(Acosta *et al.*, 2013) that may contribute to tissue fibrosis and cancer progression(Acosta *et al.*, 2013; Lunyak, Amaro-Ortiz and Gaur, 2017).

The detrimental effects of accumulating senescent cells on tissues have long been recognized(Campisi, 2013); this contributes to biological aging, tissue degeneration, and cancer(Muñoz-Espín and Serrano, 2014). Pro-inflammatory molecules and degrading enzymes in the SASP contribute to cancer progression through recruitment and differentiation of other stromal cells(Rodier and Campisi, 2011), increased proliferation, motility, and invasiveness of cancer cells(Mathon and Lloyd, 2001), and remodeling of the extracellular matrix (ECM) to promote cancer cell invasion and metastasis(Muñoz-Espín and Serrano, 2014). In previous studies senescent stromal cells enhanced the growth and malignant transformation of mammary epithelial cells(Krtolica *et al.*, 2001), promoted more rapid growth of malignant tumors(Liu and Hornsby, 2007), and caused tumor dormancy and treatment resistance when they were cannibalized by breast cancer cells (BCCs)(Bartosh *et al.*, 2016). Furthermore, non-motile BCCs treated with SASP factors (including IL-6, IL-8, and senescent fibroblast conditioned media) underwent dramatic cytoskeletal reorganization as they

transitioned to more aggressive migratory phenotypes(Aifuwa *et al.*, 2015). SASP factors also stimulated the migration of cancer cells in 2D(Ortiz-Montero, Londoño-Vallejo and Vernot, 2017) and branching of tumor organoids in 3D collagen gels(Parrinello *et al.*, 2005). Senescence is also associated with enhanced exosome secretion(Kadota *et al.*, 2018); in fact, senescence-associated exosomes are potent SASP factors that transfer inflammatory cytokines, miRNAs, and receptors important in breast cancer progression(Lehmann *et al.*, 2008). The SASP has also been shown to alter ECM remodeling to drive pulmonary fibrosis(Cárdenes *et al.*, 2018) and age-related muscle decline(Stearns-Reider *et al.*, 2017). The effect of matrix stiffening on tumor progression is widely recognized(Paszek *et al.*, 2005), and carcinoma-associated ECM considered an integral feature of malignant breast cancers(Levental *et al.*, 2009; Luo *et al.*, 2015). The increased stiffness induces a malignant phenotype in epithelial cells(Paszek *et al.*, 2005), promotes tumor progression(Levental *et al.*, 2009), and is critical for the generation and maintenance of CAFs(Calvo *et al.*, 2013). Multiple studies have investigated pro-inflammatory and immunomodulatory effects of senescent MSCs on tissues(Turinetto, Vitale and Giachino, 2016; Lunyak, Amaro-Ortiz and Gaur, 2017).

In this study, we investigated senescence-induced changes in their matrix remodeling phenotype. Senescent MSCs were larger and less motile with dense actin stress fibers and focal adhesions throughout. These changes severely limited their ability to polarize and migrate in both 2D and 3D environments. Molecular pathways that regulate cell biophysical properties and ECM remodeling were highly dysregulated, and key proteins involved in matrix stiffening upregulated, including lysyl oxidase (LOX), periostin (POSTN), and multiple collagen isoforms. Senescent MSCs also deposited and cross-linked ECM proteins altering the architecture and mechanics of the surrounding collagen network. To study the heterotypic interaction of senescent MSCs with BCCs we developed a 3D matrix-interface model which allowed for quantitative analysis of single cell migration from spheroids into the surrounding ECM. Although senescent MSCs were far less motile than pre-senescent MSCs, they continued to deposit and crosslink the collagen network to alter the behavior of BCCs. Matrix remodeling by senescent MSCs was associated with increased proliferation and motility of BCCs. Molecular inhibitors targeting senescence-induced matrix remodeling diminished this invasive BCC phenotype. These findings demonstrate the critical role senescence-induced matrix remodeling may play in age-related cancer progression.

Results

Senescent MSCs were larger with altered cytoskeletal and focal adhesion organization

Early passage pre-senescent MSCs were treated with 15 Gy γ -irradiation using Mark I 68A ^{137}Cs Irradiator (Marthandan *et al.*, 2016) to induce senescence. After ten days, senescence was confirmed based on increased expression of senescence associated- β galactosidase enzyme and reduced incorporation of BRDU (**Supplementary Figure 1A-B**). Additionally, we confirmed gene expression panel of previously described SASP markers including cell cycle regulatory factors P16 and APO1, and pro-inflammatory cytokines IL6, IL8 and IL1 β in the senescent MSCs using qRT-PCR (**Supplementary Figure 1C**). Enlarged size and irregular shape are key features of senescent cells; thus, we investigated how the cell and nuclear organization were altered in senescent vs. pre-senescent MSCs (**Figure 1A-B**). The morphological analysis showed dramatic increase in both the cell (>4 fold) and nuclear area (>2 fold) (**Figure 1B**). Immunostaining for actin and vinculin illustrated that senescent MSCs had poorly organized actin structure with focal adhesions distributed throughout the cells, not localized to the tips of actin stress fibers, as seen in pre-senescent MSCs (n>15 cells) (**Figure 1A**). Image analysis was used to quantify differences in adhesive polarity based on the location of vinculin-stained focal adhesions. For pre-senescent MSCs, focal adhesion size increased linearly with distance from the centroid with the largest focal adhesions near the cell cortex (**Figure 1C**). In contrast, focal adhesion size was independent of distance from the centroid and larger focal adhesions were often found closer to the centroid in senescent MSCs (**Figure 1C**). Furthermore, F-actin structure analysis confirmed larger actin stress fibers appeared in senescent MSCs (~10% increase) (**Figure 1C**). These changes in cytoskeletal architecture may contribute to altered mechanical properties in the cell, which regulate dynamic cell processes such as migration.

Reduced heterogeneity in cytoskeletal and nuclear mechanics

Intracellular particle tracking was used to determine the local mechanical properties of the cytoplasm from the thermal displacements of particles embedded in the cell. This technique uses video tracking technology to probe the motion of fluorescent nanoparticles over short time periods (less than 1 minute). The time-dependent particle mean squared displacements (MSDs) can easily be related to local mechanical properties of the surrounding fluid or ensemble-averaged to determine bulk mechanical properties (Tseng, Kole and Wirtz, 2002; Dawson *et al.*, 2014). In a purely viscous fluid, particles move diffusively with MSDs that vary linearly with time; however, when particles are embedded in a viscoelastic fluid like the cell cytoplasm, particle motion is much more restricted due to entrapment in the surrounding structure, and MSD slopes become less than 1. Since these mechanical properties are

determined from the transport rates of hundreds of individual particles, intracellular particle tracking can be used to probe for intracellular heterogeneity based on the variation in particle transport rates. The resulting distribution in MSDs offers insight into the degree of mechanical heterogeneity and can be connected to the spatial distribution of actin crosslinking and subcellular microstructure (Kole *et al.*, 2005). Intracellular particle tracking was used to quantify differences in cytoskeletal mechanics ($n > 15$ cells/group, 10-20 particles/cells, $n > 200$ particles/group) for pre-senescent and senescent MSCs (**Figure 1D**) based on our previously established protocols (McGrail *et al.*, 2012; Ghosh *et al.*, 2014). The amplitude and logarithmic slope ($\alpha \sim 1$) of MSDs for both population of MSCs indicated that the particle motions are less restricted in the cytoplasm suggesting viscoelastic behavior of the cytoplasmic network is dominated by viscous properties similar to our previously reported values in MSCs and metastatic cancer cells (McGrail, McAndrews and Dawson, 2013; Dawson *et al.*, 2014). The ensemble averaged MSDs (indicated by dark lines) were comparable between pre-senescent and senescent MSCs, indicating similarity in their bulk mechanical properties; however, the reduced heterogeneity in individual particle MSDs for senescent MSCs suggests their mechanical properties are more homogeneous than pre-senescent MSCs (**Figure 1D**). This reduced heterogeneity in cytoskeletal mechanics is further illustrated by reduced coefficient of variation (CV) in MSD values at time scales $t=1$ and 10s (**Figure 1D**).

Particle tracking of Hoechst-labeled chromatin granules was used to probe for differences in nuclear mechanics (Figure 1E) (Xuan *et al.*, 2018). At short time scales, the MSDs remained constant; whereas, at longer time scales, the MSDs varied linearly with time for both cell types. This inflection point represents a transition from elastic to viscous fluid properties that is referred to as the relaxation point. Again, we see little difference in the ensemble averaged MSDs for both groups with less variation in individual particle MSDs for senescent MSCs (**Figure 1E**). This reduced heterogeneity in particle transport rates was significant at long time scales after the relaxation had occurred. This data indicates the bulk nuclear mechanical properties of senescent MSCs are similar albeit more homogeneous in comparison to pre-senescent MSCs. Interestingly, the relaxation point was significantly reduced in senescent MSCs (**Supplementary Figure 1D**), signifying a faster transition to a softer nucleus, suggesting some fundamental difference in nuclear deformation.

Senescent MSCs lost their migratory capacity

Next, we investigated how alterations in cell structure affect dynamic cell processes such as migration. We tracked 2D migration of over 500 cells per condition and found senescent MSCs to be significantly less motile than pre-senescent MSCs (**Figure 2A**). In addition to reduced motility, senescent MSCs also moved less directionally. Migration of MSCs in 3D collagen gels

followed a similar trend; the mean velocity of pre-senescent MSCs was more than 2-fold higher than senescent MSCs (**Figure 2B**). Mesenchymal migration in 3D collagen gels is characterized by the formation of integrin-based adhesions and dendritic protrusions at the cell's leading edge, followed by nuclear elongation in the direction of migration, and branching of protrusions to support the migration of polarized cells along collagen fibers (Wu, Gilkes and Wirtz, 2018). Both cell types formed integrin-based adhesions and dendritic protrusions; however, only pre-senescent MSCs were able to polarize these protrusions for directional cell migration (**Figure 2B**). We quantified this observation based on the ratio of leading edge to trailing edge protrusions. For senescent MSCs, this ratio was approximately 1, further demonstrating the loss in cell polarity with senescence. This ratio was increased up to 50% for pre-senescent MSCs, in part to the large number of migrating cells (**Figure 2B**). In addition to the polarized binding and the formation of adhesive protrusions at the cell's leading edge, the ability for cells to migrate in 3D environments is largely regulated by nuclear size, shape, and rigidity (Wolf *et al.*, 2003). Senescent MSCs had larger but slightly more elongated nuclei than pre-senescent MSCs. Thus, the nuclear shape factor of senescent MSCs was reduced (**Figure 2C**). However, pre-senescent MSCs more readily altered their nuclear shape (Δ NSF) allowing them to squeeze through smaller pores. This is further illustrated by their lower feret diameters since the minimum feret diameter represents the smallest pore size an elongated nucleus can squeeze through (**Figure 2C**). Overall, the loss of migration of senescent MSCs correlated with their larger and less deformable nuclei and inability to adjust cell polarity sufficiently to move in confined collagen-rich environments.

Senescence induced wide scale differences in protein expression

To understand the senescence induced molecular changes in MSCs, a mass spectrometry-based proteomics analysis was carried out. 1134 unique proteins were significantly regulated in senescent MSCs compared to pre-senescent MSCs. Of these differentially altered proteins 116 were related to nuclear or cytoskeletal structure. A small number of significantly downregulated (green) and upregulated (red) proteins were listed (**Figure 3A, Supplementary Figure 2**). Actin binding proteins that increase the stability of actin cytoskeleton were upregulated with senescence; this included cortactin (CTTN), alpha actinin (ACTN2), and adducins (ADD1/3). We previously reported similar changes in actin binding protein expression in TGF- β 1 treated MSCs, which resulted in homogeneous stiffening of the cytosol and development of CAF-like phenotype (Ghosh *et al.*, 2014). Also, proteins that control microtubule dynamics including, microtubule associated proteins (MAPRE1 (EB1), MAP1B, MAP4) were collectively downregulated in senescent MSCs. Additionally, proteins that control the dynamics of nuclear structure, including LINC complexes (SUN2), nuclear lamina (LMNB1, LBR), nuclear matrix (MATR3), and nuclear pore complexes (IPO7, IPO11)

were downregulated in senescent MSCs. Loss of LMNB1 has been associated with cellular senescence and biological aging (Dahl *et al.*, 2006). While the expression of integrins (ITGA2, ITGB5, ITGB1) and focal adhesion proteins (VCL) was increased, cell-cell adhesion molecules (ALCAM, MCAM) were downregulated (**Figure 3B**). Furthermore, ERM proteins (EZR, MSN) that link the cytoskeleton to the plasma membrane and transfer signals to regulate polarization in adhesion dependent processes and membrane dynamics were downregulated. Altogether, these results further support the idea that senescence results in less dynamic cytoskeletal structure which is not capable of cell polarization to drive cell motility.

Interestingly, a significant number of proteins related to ECM synthesis and turnover were differentially expressed in senescent vs. pre-senescent MSCs (**Figure 3B**). These ECM proteins included multiple collagen isoforms (COL14, COL1, COL6) and laminins (LAMC1, LAMB1) found in the basement membrane. Fibril-associated collagens like COL14 are scaffolding collagens that contribute to the formation of dense ECM. COL6 is a non-fibrillar collagen important in matrix assembly and fibroblast motility in the skin (Theocharidis *et al.*, 2016). Additionally, upregulation of matrix proteinases (MMP2), matrix proteinase inhibitors (TIMP1, TIMP3), crosslinkers (TGM2, LOX), and matricellular proteins (POSTN, THBS1, VTN) suggest that senescent MSCs actively remodel the local microenvironment.

Senescent MSCs remodeled the surrounding collagen matrix

Multiphoton microscopy was used to image collagen fibers surrounding CFSE-labeled MSCs (**Figure 4A**). Image analysis of 3D cell volume revealed that senescent MSCs were over 3-fold larger than pre-senescent MSCs (**Figure 4B**). Both pre-senescent and senescent MSCs remodeled the local ECM which resulted in differences in the local collagen architecture. To quantify the architecture of collagen surrounding cells, SHG images were analyzed using CurveAlign to calculate fiber properties including density and alignment. The coefficient of alignment that varies between 0 to 1 for isotropic material to perfectly aligned matrix, was higher for senescent MSCs compared to pre-senescent MSCs (**Figure 4B**), indicating that collagen was aligned along cell surface. Additionally, collagen density around senescent MSCs was increased as indicated by the higher box density. Overall, senescent MSCs displayed increased volume with a larger surface area for cell-ECM interactions and significantly remodeled the surrounding matrix.

Both pre-senescent and senescent MSCs uniquely contributed to BCC invasion.

To study the heterotypic interaction of MSCs with BCCs, we developed a 3D matrix-interface model that allowed for quantitative analysis of single cell migration from spheroids into surrounding ECM. Since MDA-MB-231 only formed dense spheroids in the presence of stromal cells, an equal number of GFP positive MDA-MB-231 cells were cultured with MSCs

in suspension to form aggregates. To mimic the presence of both pre-senescent and senescent MSCs in the tumor, we created an additional mixed group with an equal number of pre-senescent and senescent MSCs. Inclusion of senescent MSCs in these cultures resulted in larger sized spherical aggregates (spheroids) (**Supplementary Figure 3A-B**). After 72 hours, the aggregates were embedded in polymerized collagen to monitor the spreading and invasion of BCCs and MSCs from spheroids over 16-hour period (**Figure 5, Supplementary Figure 3**). Senescent MSCs alone or in the mixed group induced an invasive BCC phenotype, characterized by an increase in spheroid size with time and increased number of protrusions after 16 hours (**Figure 5B, Supplementary Figure 4A**). Next, we quantified both the number of MSCs and BCCs escaping from spheroids (**Figure 5C-D**). An interesting aspect to emerge from this study was the propensity of pre-senescent MSCs to invade the collagen gels (highlighted with the yellow cells in **Figure 5C**). While pre-senescent MSCs invaded the matrix more rapidly with higher numbers, senescent MSCs promoted BCC invasion into collagen (highlighted with red cells in **Figure 5C**). Presence of both attributes in the mixed population resulted in the highest level of both MSC and BCC invasion (**Figure 5, Supplementary Figure 3D**).

Matrix remodeling abilities of MSCs were crucial for BCC invasion

To further understand the organization of the cells in the spheroid and its interaction with the surrounding collagen matrix, multiphoton microscopy was used to image NucRed-labeled cells (both MSCs and BCCs) by fluorescence (shown in red) and collagen fibers by second harmonic generation (SHG) (shown in cyan) (**Figure 6A**). The overlays of the average intensity projections highlight differences in cell density and packing between pre-senescent and senescent MSC containing spheroids (**Figure 6A, Supplementary Figure 4C**). Mobilization of the pre-senescent MSCs into the surrounding collagen correlated with spheroid cores becoming more hollow; whereas, spheroids cultured with senescent MSCs remained relatively solid (**Figure 6A, Supplementary Figure 5**). To quantify the architecture of surrounding collagen gels, SHG images were analyzed using CurveAlign to calculate fiber properties including alignment, and width. Coefficient of alignment that varies between 0 to 1 for isotropic material to perfectly aligned matrix, was higher in spheroids with pre-senescent and mixed MSC populations compared to senescent MSCs (**Figure 6B, Supplementary Figure 4**). Average collagen fiber width was higher in senescent MSCs suggesting more matrix bundling and/or crosslinking (**Figure 6C**). Previous studies have found more collagen crosslinking with aging (Frantz, Stewart and Weaver, 2010; Phillip *et al.*, 2015). Pre-senescent MSCs that readily migrated into the collagen may lead the way causing fiber alignment; whereas, non-motile senescent MSCs can promote crosslinking of collagen surrounding the spheroid promoting stiffer local regions.

Finally, we probed if the disruption of the MSC mediated matrix remodeling could diminish the invasive behavior of BCCs in 3D. MMP activity was blocked by inhibitor GM6001; whereas, LOX was blocked using BAPN. Additionally, POSTN antibody was used to determine if the increased expression of this matricellular protein was a contributing factor to the more invasive BCC phenotype. After 16 hours, GM6001, BAPN, and POSTN-Ab abrogated cell invasion to different degrees (**Figure 7A-C**). GM6001 was most efficient and completely able to block spheroid growth and individual BCC invasion for both pre-senescent and senescent MSC containing spheroids. Blocking LOX and POSTN did not affect the spheroids with pre-senescent MSCs; however, these blocking strategies resulted in decreased invaded area for spheroids with post-senescent MSCs. BAPN and POSTN-Ab were also able to partially block the individual cell invasion ($p=0.052$ for BAPN, $p=0.083$ for POSTN Ab).

Discussion

Cellular senescence is a critical mechanism of limiting abnormal growth and cancer development; however, senescent cells accumulating in tumors can profoundly alter the biophysical properties of the tissue to force cancer progression toward malignancy. MSCs are present throughout vascularized tissues and survive for many years *in vivo* (Fehrer and Lepperdinger, 2005); this increases their risk for developing DNA damage from ionizing radiation, environmental toxins, and chemotherapy, which can trigger senescence. Previous studies show bone marrow derived MSCs transition to a CAF phenotype after exposure to MDA-MB-231 breast cancer cells (BCCs) (Mishra *et al.*, 2008; Shangguan *et al.*, 2012) and promote breast tumor growth (Karnoub *et al.*, 2007; Lacerda *et al.*, 2015). However, limited data is available to demonstrate the impact of senescence on MSC function in the tumor.

MSC senescence results in increased expression of ECM proteins and matrix modifying enzymes, which can alter the composition and architecture of tissue environments to promote cancer progression. At low cell densities, this effect would only alter local regions of the collagen matrix; however, as senescent cells accumulate with age or genotoxic stress, this local matrix-remodeling effect may lead to abnormal collagen architectures and bulk matrix-stiffening effects. Changes in cell biophysical properties are essential in the development of this matrix remodeling phenotype. This is because cells sense and respond to forces from the ECM through mechanosensitive molecules in the cytoskeleton (Wang, Tytell and Ingber, 2009). The cytoskeletal proteins important in this process were highly dysregulated in senescent MSCs. Actin stress fibers formed by bundling and cross-linking of actin filaments (CTTN, ACTN, ADD) were dramatically increased and microtubule-binding proteins (EB1, MAPs) that regulate the dynamic structure of microtubules were downregulated (**Figure 1, Supplementary Figure 2**). These results correlated with significantly reduced heterogeneity

in intracellular mechanics in senescent MSCs, suggesting the microstructure of this polymeric network is more homogeneous after senescence (**Figure 1D**). Rapid remodeling of the cytoskeletal structure to maintain contractile cell phenotype is an energy intensive process(Phillip *et al.*, 2015). Thus, more stable mechanical properties may contribute to the progressive metabolic alterations in senescent cells which also require significant energy to maintain high production of SASP factors. These cytoskeletal changes may contribute to the larger and more stable size of senescent MSCs and may also explain how non-proliferating cells are able to remain viable in the tissues for long periods of time. On the other hand, a less dynamic cytoskeletal network may limit the cell's ability to respond to external stimuli, since differences in cell tension are important in transferring signals from the external environment to the nuclear lamina. Nuclear mechanics is mainly controlled by the structure of the nuclear lamina, along with underlying chromatin organization(Phillip *et al.*, 2015; Stephens *et al.*, 2017). Our proteomics analysis revealed HDAC and other histone cluster proteins were collectively downregulated in senescent MSCs (**Supplementary Figure 2**); the reduced expression of histone-modifying proteins in senescent MSCs may correlate with their faster transition from elastic to viscous nuclear mechanics(Stephens *et al.*, 2017). Nuclear lamina proteins LMNB1 and LBR were significantly downregulated in senescent MSCs. The reduced expression of LMNB1 and LBR has been associated with loss of peripheral compact heterochromatin and wide-scale changes in DNA condensation that can correlate with the reduced heterogeneity in nuclear mechanics of senescent MSCs(Swanson *et al.*, 2015; Criscione, Teo and Neretti, 2016). Ferrera *et al.* reported reduced heterogeneity in nuclear stiffness in quiescent human skin fibroblasts compared to proliferating cells(Ferrera *et al.*, 2014). While B-type lamins contribute to elastic resistance of the cells, Lamin A (LMNA) has been associated with deformation-resistant viscous stiffness(Gruenbaum and Foisner, 2015; Lele, Dickinson and Gundersen, 2018). Increased LMNA expression correlated with less deformable nucleus(Harada *et al.*, 2014). In our senescent MSCs, a combination of LMNB1 downregulation and LMNA upregulation (Supplementary Figure 2D) correlated with elongated but less deformable nuclei.

Higher ratios of lamin A to lamin B has been shown to reduce nuclear deformability to inhibit cancer cell migration through pores(Swift *et al.*, 2013; Harada *et al.*, 2014). These overall changes in cytoskeletal and nuclear organization and mechanics can profoundly alter cell migration. Polarization of cytoskeletal and perinuclear actin results in anisotropy in actin structure and cytoskeletal tension, which both contribute to nuclear deformation and cell migration(Wu, Gilkes and Wirtz, 2018). This structure is also dynamic, which allows cells to sense and respond to stimuli important in directing adhesion and motility(Wang, Tytell and Ingber, 2009; Lee and Kumar, 2016). Although cell adhesion molecules and focal adhesion

proteins are upregulated with senescence, these adhesion complexes remain distributed throughout senescent MSCs instead of being localized to the leading edge as seen in pre-senescent MSCs (**Figure 2**). This inability to polarize adhesive protrusions was associated with uniformly slower migration in both 2D and 3D systems (**Figure 2-3, Supplementary Figure 2**). However, migration of MSCs was more reduced in 3D compared to 2D. In 3D tissue microenvironments, nuclear deformation is also essential for cell migration through pores that are often smaller than the nondeformed nucleus (Friedl, Wolf and Lammerding, 2011). The nuclei of senescent MSCs were larger (ferret diameter $\sim 7\text{-}11\ \mu\text{m}$) than the size of collagen pores ($d \sim 6\text{-}7\ \mu\text{m}$) (Banerjee *et al.*, 2008). With increased collagen concentration, the cell migration will become more inhibited as pore size will decrease (Wolf *et al.*, 2009). Reported pore sizes in normal and cancer tissues are much smaller albeit with high degree of variation and will likely further limit the migration of the senescent cells *in vivo*.

Senescent MSCs continue to deposit and crosslink collagen in the surrounding matrix, but because they are less motile, this may lead to the formation of a highly dysregulated collagen network surrounding senescent cells (**Figure 3**). The upregulation of MMP inhibitors (TIMPs) and crosslinking agents (transglutaminase and LOX) suggests that senescent MSCs will increase the rigidity of the surrounding matrix. The ECM proteins upregulated in senescent MSCs were also consistent with ECM alterations seen in more invasive breast cancers (Abbott *et al.*, 2008). High expression of these ECM proteins corresponded with reduced disease-survival in patients with basal subtype of breast cancer (**Supplementary Figure 7**). Among these ECM proteins, the increased expression of matricellular protein POSTN has been associated with increased metastasis and poor survival in invasive breast cancer patients (Kim *et al.*, 2017; Ratajczak-Wielgomas *et al.*, 2017). It is also highly expressed in both cancer cells and CAFs of invasive ductal breast carcinomas (Ratajczak-Wielgomas *et al.*, 2016). POSTN was upregulated in both 2D and 3D cultures of senescent MSCs, suggesting that senescent MSCs contribute to aggressive breast tumor phenotypes through the upregulation of this matricellular protein. Interestingly, other positive markers of CAFs including α -SMA, FAP and VIM were also upregulated in senescent MSCs (Tao *et al.*, 2017).

We created a 3D matrix interface model that not only allows direct heterotypic interactions between MSCs and BCCs but also enables us to monitor both single and collective cell invasion and surrounding matrix remodeling. MSCs and BCCs distributed in cell solution self-organized in spheroid cultures with MSCs at the core and BCCs at the periphery. Over time, pre-senescent MSCs migrated out of the core and were more equally distributed throughout these cultures; however, senescent MSCs remained at the spheroid core structurally supporting the spheroid growth and secreting ECM proteins to remodel the surrounding matrix. This spontaneous reorganization of mixed cell populations into aggregates of similar cells has

been demonstrated in co-cultures of invasive and non-invasive breast cancer cells(Oswald *et al.*, 2017) and embryonic tissues(Amack and Manning, 2012) and is thought to be mediated by homo-or hetero-typic cadherin interactions(McAndrews, Yi, *et al.*, 2015). While cadherin-mediated interactions can drive the initial sorting, the reduced motility of senescent MSCs is likely responsible for keeping these cells at the spheroid core. Our mosaic confocal images demonstrated that spheroids formed from senescent MSCs are tightly packed in part to the high number of senescent MSCs that remain viable at the spheroid core (**Supplementary Figure 5**). Analyzing the mosaics of confocal images, it became increasingly clear that changes in cellular shape from core to the periphery of the spheroids is highest for spheroids formed with senescent MSCs (**Supplementary Figure 6**). Cells at the periphery were more elongated with fewer cell-cell contacts and higher variation in cell shape factors; this is in contrast to cells at the core, which were tightly packed in circular shapes with reduced variation in cell shape akin to a jammed state (Dolega *et al.*, 2017; Oswald *et al.*, 2017). This distribution of cell shape is consistent with high solid stress at the core and cells at the perimeter transitioning to more invasive cancer cell phenotype. Conversely, pre-senescent MSCs maintained their highly motile phenotype and rapidly moved into the surrounding collagen gel leaving a hollow core behind, suggesting that cells remaining at the core of these spheroids would reside in a relatively unjammed state. Haeger *et al.* have shown that jammed state in confined tissue e.g. densely packed group of cells in tracks created by leader cells, promoted collective invasion of mesenchymal tumor(Haeger *et al.*, 2014). In our model, tracks created by migrating pre-senescent MSCs can be used by jammed BCCs and senescent cells to allow collective invasion.

Other studies have demonstrated that fibroblast remodeling of the matrix generates tracks for cancer cells to follow promoting cancer cell invasion and metastasis(Gaggioli *et al.*, 2007). The coefficient of alignment of the surrounding collagen for pre-senescent MSC spheroid was very similar to the alignment coefficient of individual pre-senescent MSCs in collagen (**Figure 4, 6**). The senescent MSCs remained at the core and were not able to directly affect the collagen surrounding the spheroid surface, which was dominated by alignment with BCCs. Although senescent MSCs were unable to move into the surrounding matrix, they clearly induced more proliferative and invasive phenotype in BCCs compared to pre-senescent MSCs. Furthermore, the invasive behavior was enhanced when BCCs were combined with a mixture of pre-senescent and senescent MSCs. This result was attributed to matrix remodeling and soluble factor secretion effects of senescent MSCs, which enhanced the migration of pre-senescent MSCs allowing them to form tracks in the collagen network for cancer cells to follow. Together, these results suggest that a mixed population of MSCs can synergistically combine the invading properties of pre-senescent MSCs and SASP/ECM remodeling properties of

senescent MSCs to facilitate BCC invasion. This is significant because senescent MSCs are likely a small population of stromal cells *in vivo*. However, senescent MSCs can transfer senescence to other stromal cells through paracrine signaling from the SASP (Severino *et al.*, 2013).

In summary, we demonstrated that senescent MSCs that accumulate in tumors alter the local and bulk mechanical properties of tissue ECM to promote more invasive breast cancer phenotypes. Understanding the interactions between senescent stromal cells and cancer cells is critical in developing new strategies for targeting age-associated cancer progression. Although these studies focused on MSCs in breast cancers, senescence-induced biophysical changes in MSCs would apply to other age-associated fibrotic diseases.

Materials and Methods

Cell culture: Human bone marrow-derived MSCs (MSCs) isolated from healthy 24-year-old female donor (8001L) were obtained from Texas A&M Cell Distribution Center. MSCs were cultured in Minimum Essential Medium Alpha (α MEM) (Corning) supplemented with 20% fetal bovine serum (FBS, Atlanta Biologicals, lot#J15102), 15mM HEPES (Fisher chemicals), 1% penicillin-streptomycin (Corning) and 1% L-glutamine (Corning). MSCs were used between passage 2-6. Triple negative human BCC line MDA-MB-231 was purchased from ATCC and cultured in DMEM and Ham's F12 mix (Corning) supplemented with 10% FBS and 1% penicillin-streptomycin. All cells were maintained at 37° C and 5% carbon dioxide as per supplier's instructions.

Irradiation: MSCs cultured to 60% confluence were exposed to 15 Gy γ -irradiation using a Mark I 68A137Cs Irradiator at a rate 5.04 Gy/min for 3 minutes. After 10 days, MSCs were assessed to confirm senescence and were subsequently used for all experiments. This model of induced senescence was selected to allow for direct comparison between pre- senescent and senescent MSCs from the same donor with large numbers of cells.

Proliferation: MSCs were cultured on glass coverslips and incubated overnight (12 hours) with 10 μ M Bromodeoxyuridine (BrdU) (Millipore Sigma). Cells were then fixed in 4% formaldehyde followed by permeabilization with 0.5% Triton X-100 in PBS. After treatment with 4N HCl, cells were blocked with 5% horse serum. Following sequential incubation with biotinylated anti-BrdU (Biolegend) primary antibody (1:100) and streptavidin conjugated Alexa Fluor 488 secondary antibody (Biolegend), the coverslips were sealed with VectaShield Mounting Medium with propidium iodide (PI) (Vector Labs) and imaged on Nikon Eclipse Ti inverted microscope at 20x magnification. For quantification, the number of BrdU+ cells (green nuclei) were normalized to the total number of cells (red nuclei).

Cell and nuclear morphology: Pre- senescent and senescent MSCs were cultured in a 24-well plate and were subsequently fixed with ice-cold methanol followed by staining with crystal violet (10mg/ml) (Carolina Biological) and DAPI (10ug/ml) (Acros Organics). To analyze cell morphology, cell boundaries were manually traced in Image-J (n>1000 cells per condition). For quantitative analysis of the nuclear area, we used automated processing of the images (n>1000 cells per condition) through CellProfiler (Broad Institute).

Immunostaining of cytoskeleton: To visualize filamentous actin and focal adhesion protein vinculin, we followed the previously described immunostaining protocol (McGrail *et al.*, 2012). Briefly, MSCs cultured on glass coverslips were fixed with 4% formaldehyde, permeabilized with Triton X-100 (0.5%), and blocked with 5% horse serum. Cells were then incubated in anti-vinculin (1:100) (Invitrogen) primary antibody followed by staining with TRITC-conjugated Phalloidin (Cytoskeleton Inc.), and Alexa Flour 488 conjugated secondary antibody (Invitrogen). Finally, samples were sealed with Vectashield Mounting Medium with DAPI. High-resolution images taken with Nikon Eclipse Ti microscope were used to analyze actin stress fibers with CT-FIRE (LOCI). Focal adhesion size and distance were processed through a custom pipeline in CellProfiler (Broad Institute). Images were thresholded and segmented using the IdentifyPrimaryObjects module. Focal adhesion area was measured using MeasureObjectSizeShape and distance was measured with RelateObjects. The centroid and minimum sub-parameter were used to measure focal adhesion distance from the centroid and edge of the cell, respectively.

Multiple Particle Tracking (MPT): To quantify differences in intracellular mechanics, thermal motion of ballistically injected 200 nm green fluorescent particles embedded in cytosol was tracked in live cells. Videos of particle motion were taken at 30 frames per second for 20 seconds using a Nikon Eclipse Ti inverted microscope and QuantEM CCD camera. Particle displacements were tracked in MATLAB based on previous established algorithms (McGrail, McAndrews and Dawson, 2013). Briefly, a band-pass filter is used to identify particles based on intensity-weighted centroids, then a Hungarian linker algorithm is used to determine traces of particle motion, and the time-dependent 2D particle mean squared displacements (MSDs) are calculated from particle motion as $\langle \Delta r^2(\Delta t) \rangle = \langle [x(t+\Delta t) - x(t)]^2 + [y(t+\Delta t) - y(t)]^2 \rangle$. For each condition an average of 15 cells with 10-20 particles per cell were analyzed for more than 200 particles per condition.

Nuclear tracking: To quantify nuclear mechanics, MSCs seeded on collagen-coated glass were labeled with Hoechst 33342. Using techniques described above for MPT, the motion of Hoechst-labeled chromatin was tracked, and the relaxation time (characterizing the transition

from elastic to viscous behavior) was determined from the logarithmic slope of the MSD(McGrail *et al.*, 2015).

Cell motility: MSCs were seeded on collagen coated 24-well plates at sub-confluent density. Cells were labeled with Hoechst 33342 live cell dye per manufacturer's instructions and then imaged on a Nikon Eclipse Ti inverted microscope equipped with an environmental chamber and maintained at 37°C and 5% carbon dioxide throughout the experiment. Images were captured every 10 minutes for up to 12 hours. Image stacks were processed in MATLAB to track the x-y coordinates of cell nuclei to determine cell velocity(McGrail *et al.*, 2015).

qRT-PCR analysis: All the reagents used for RNA isolation, cDNA synthesis and qRT-PCR were purchased from BioRAD. Total mRNA was extracted from the MSCs with PureZOL RNA isolation reagent according to the manufacturer's protocol. Using Nanodrop 1000, the purity and integrity of the RNA was assessed and subsequently cDNA was synthesized using iScript cDNA synthesis kit. 1ug of RNA was converted to cDNA followed by real-time PCR for senescence markers:

APO1: F: CAAATGTCTATCCACAGGCTAACCC

R: AGAGGTAATTTAGAGGCAAAGTGGC

P16: F: CACTCACGCCCTAAGC

R: GCAGTGTGACTCAAGAGAA

IL6: F: CCAGGAGCCCAGCTATGAAC

R: CCCAGGGAGAAGGCAACTG

IL8: F: GAGTGGACCACACTGCGCCA

R: TCCACAACCCTCTGCACCCAGT

IL1β: F: TGCACGCTCCGGGACTCACA

R: CATGGAGAACACCACTTGTTGCTCC

18s: F: CGCCGCTAGAGGTGAAATTC

R: TTGGCAAATGCTTTTCGCTC

Proteome Analysis: Pre-senescent and senescent MSCs cultured in T-175 flasks were trypsinized and centrifuged at 700g for 10 minutes to pellet the cells. Cell pellets were suspended in 30 μL PBS and flash frozen in liquid nitrogen before transferring on dry ice to Brown University's Proteomics Core Facility for protein analysis (n=4). To select peptides that

show a statistically significant change in abundance between pre-senescent and senescent MSCs, q-values for multiple hypothesis tests were calculated based on p-values from two-tailed unpaired Student's t tests using the R package QVALUE. The values reported here are log₂ transformed fold change in senescent MSCs compared to pre-senescent MSCs.

Pathway analysis: Pathway analysis & visualization was carried out using web based-tool Metaboanalyst 3.0 using the KEGG (www.genome.jp/kegg/) pathway database(Chong *et al.*, 2018). Significantly regulated peptides from proteomic analysis were used separately to identify most significantly regulated pathways.

3D collagen gels: Pre-senescent and senescent MSCs were harvested and suspended in collagen I (corning) solution at final concentration of 1.5mg/ml and plated on a 96 well-plate as per previous protocol(McAndrews, McGrail, *et al.*, 2015). Collagen gels were polymerized on ice for 45 minutes followed by incubation in 37°C for 2 hours. After adding media, gels were immediately moved to the microscope to capture images every 15 minutes for up to 12 hours. Number of protrusions were manually analyzed using FIJI (Image J). Image stacks were processed in MATLAB to track the x-y coordinates of cell nuclei to determine cell velocity(McGrail *et al.*, 2015).

Matrix-interface model: GFP positive MDA-MB-231 cells were mixed at an equal ratio with three groups of MSCs - pre-senescent, senescent, or 1:1 mixture of pre-senescent and senescent MSCs. Then, the cell solutions were seeded on top of agarose coated 96-well plate at a density of 2000 cells/well to stimulate cell aggregate formation in DMEM/F12 media supplemented with 10% FBS and 1% penicillin and streptomycin. Cell aggregates were harvested after 72 hours and spun down briefly to recollect them in serum free media. Aggregates were then suspended in collagen I (Corning) solution at final concentration of 1.5mg/ml and plated on a 96 well-plate as per previous protocol(McAndrews, McGrail, *et al.*, 2015). Collagen gels were polymerized on ice for 45 minutes followed by incubation in 37°C for 2 hours. After adding media, gels were immediately moved to the microscope to capture images every 10 minutes for up to 16 hours. Spheroid area, cell numbers, and cell distance from spheroid boundary were manually analyzed in Nikon elements software. Number of protrusions were calculated using previously published MATLAB algorithm(Hou *et al.*, 2018).

Second Harmonic Generation (SHG) imaging of collagen gels: Multiphoton microscopy was used to image 3D collagen gels by SHG(Perentes *et al.*, 2009); collagen fibers are an efficient source of SHG in part to their crystalline structure, and multiphoton microscopy can be used for simultaneous imaging of collagen (by SHG) and MSCs (stained with NucRed). Spheroids embedded in collagen gels for 16 hours were fixed in 4% formaldehyde and incubated with NucRed; after washing with PBS, collagen gels immobilized using an agarose mold before

mounting on coverslips. Olympus multiphoton microscope with 810 nm excitation and 405 nm emission filters and 25x water immersion lens was used to obtain 3D image stacks (up to 100 μm thick with 1 μm separation distance). Multiple parameters were quantified for each slice of the acquired stack using CurveAlign4.0 (Bredfeldt *et al.*, 2014). Here we analyzed coefficient of alignment based on the orientation of collagen fibers in an image. For single cell analysis, cell boundaries were traced manually and uniform outward dilation of 50 μm along the cell outline was used to determine the local fiber properties surrounding the cells including, coefficient of alignment and density. For spheroid image stacks, alignment and density were calculated for uniform size boxes (locally) and over entire image. Additionally, CT-FIRE module was used to measure fiber properties including length and width for the collagen around spheroids.

Inhibitor studies: BCC spheroids with the mixed population of pre-senescent and senescent MSCs were treated with inhibitors. Small molecule inhibitor and antibody stocks were prepared in dimethyl sulfoxide (DMSO) and PBS, respectively. All inhibitors were further diluted to final concentration in serum-free media. To disrupt ECM reorganization the following inhibitors were used: pan-MMP inhibitor GM-6001 (20 μM) (Cayman Chemicals), LOX inhibitor β -Aminopropionitrile (BAPN) (20 μM) (Cayman Chemicals), and Periostin antibody (2.5 $\mu\text{g}/\text{ml}$) (Sigma).

Statistics: All assays were performed with minimum of 3 replicates and the results are reported here as mean \pm standard error of the mean. Statistical analysis using Student's *t* test was utilized for comparison between groups with p-value less than 0.05 considered as significant (* $p < 0.05$, ** $p < 0.01$, *** $p < 0.001$).

Acknowledgements

This work was funded by grants from the National Science Foundation (1825174) and National Institute of Health NIGMS (P30 GM110750) and National Science Foundation Graduate Research Fellowship for C.M.P. and T32 Grant (HL134625) for N.Q. We would like to thank Genomics and Proteomics core facility for their support and expertise especially Dr. Nagib Ahsan.

Author contributions

This study was designed by M.R.D. and D.G.; D.G. and C.M.P. performed the experiments; D.G., N.Q., B.X., and A.H.L. analyzed the data and generated figures; M.R.D. and D.G. wrote the paper.

References

- Abbott, K. L. *et al.* (2008) 'Targeted glycoproteomic identification of biomarkers for human breast carcinoma.', *Journal of proteome research*. NIH Public Access, 7(4), pp. 1470–80. doi: 10.1021/pr700792g.
- Acosta, J. C. *et al.* (2013) 'A complex secretory program orchestrated by the inflammasome controls paracrine senescence', *Nature Cell Biology*, 15(8), pp. 978–990. doi: 10.1038/ncb2784.
- Aifuwa, I. *et al.* (2015) 'Senescent stromal cells induce cancer cell migration via inhibition of RhoA/ROCK/myosin-based cell contractility.', *Oncotarget*. Impact Journals, LLC, 6(31), pp. 30516–31. doi: 10.18632/oncotarget.5854.
- Alessio, N. *et al.* (2015) 'Low dose radiation induced senescence of human mesenchymal stromal cells and impaired the autophagy process', *Oncotarget*. Impact Journals, 6(10), pp. 8155–8166. doi: 10.18632/oncotarget.2692.
- Amack, J. D. and Manning, M. L. (2012) 'Knowing the boundaries: extending the differential adhesion hypothesis in embryonic cell sorting.', *Science (New York, N.Y.)*. American Association for the Advancement of Science, 338(6104), pp. 212–5. doi: 10.1126/science.1223953.
- Banerjee, P. *et al.* (2008) 'A novel and simple cell-based detection system with a collagen-encapsulated B-lymphocyte cell line as a biosensor for rapid detection of pathogens and toxins', *Laboratory Investigation*. Nature Publishing Group, 88(2), pp. 196–206. doi: 10.1038/labinvest.3700703.
- Bartosh, T. J. *et al.* (2016) 'Cancer cells enter dormancy after cannibalizing mesenchymal stem/stromal cells (MSCs)', *Proceedings of the National Academy of Sciences*, 113(42), pp. E6447–E6456. doi: 10.1073/pnas.1612290113.
- Bredfeldt, J. S. *et al.* (2014) 'Computational segmentation of collagen fibers from second-harmonic generation images of breast cancer.', *Journal of biomedical optics*. Society of Photo-Optical Instrumentation Engineers, 19(1), p. 16007. doi: 10.1117/1.JBO.19.1.016007.
- Calvo, F. *et al.* (2013) 'Mechanotransduction and YAP-dependent matrix remodelling is required for the generation and maintenance of cancer-associated fibroblasts.', *Nature cell biology*. Nature Publishing Group, 15(6), pp. 637–646. doi: 10.1038/ncb2756.
- Campisi, J. (2013) 'Aging, Cellular Senescence, and Cancer', *Annual Review of Physiology*. Annual Reviews, 75(1), pp. 685–705. doi: 10.1146/annurev-physiol-030212-183653.

- Caplan, A. I. and Dennis, J. E. (2006) 'Mesenchymal stem cells as trophic mediators', *Journal of Cellular Biochemistry*, pp. 1076–1084. doi: 10.1002/jcb.20886.
- Cárdenes, N. *et al.* (2018) 'Senescence of bone marrow-derived mesenchymal stem cells from patients with idiopathic pulmonary fibrosis.', *Stem cell research & therapy*. BioMed Central, 9(1), p. 257. doi: 10.1186/s13287-018-0970-6.
- Carey, S. P., Martin, K. E. and Reinhart-King, C. A. (2017) 'Three-dimensional collagen matrix induces a mechanosensitive invasive epithelial phenotype', *Scientific Reports*, 7. doi: 10.1038/srep42088.
- Chong, J. *et al.* (2018) 'MetaboAnalyst 4.0: towards more transparent and integrative metabolomics analysis', *Nucleic Acids Research*. Narnia, 46(W1), pp. W486–W494. doi: 10.1093/nar/gky310.
- Criscione, S. W., Teo, Y. V. and Neretti, N. (2016) 'The Chromatin Landscape of Cellular Senescence.', *Trends in genetics : TIG*. NIH Public Access, 32(11), pp. 751–761. doi: 10.1016/j.tig.2016.09.005.
- Dahl, K. N. *et al.* (2006) 'Distinct structural and mechanical properties of the nuclear lamina in Hutchinson-Gilford progeria syndrome', *Proceedings of the National Academy of Sciences*, 103(27), pp. 10271–10276. doi: 10.1073/pnas.0601058103.
- Dawson, M. R. *et al.* (2014) 'Intracellular Particle Tracking Microrheology', in *Handbook of Imaging in Biological Mechanics*. CRC Press, pp. 381–388.
- Dolega, M. E. *et al.* (2017) 'Cell-like pressure sensors reveal increase of mechanical stress towards the core of multicellular spheroids under compression', *Nature Communications*. Nature Publishing Group, 8, p. 14056. doi: 10.1038/ncomms14056.
- Farias, V. de A. *et al.* (2015) 'Human mesenchymal stem cells enhance the systemic effects of radiotherapy', *Oncotarget*, 6(31). doi: 10.18632/oncotarget.5216.
- Fehrer, C. and Lepperdinger, G. (2005) 'Mesenchymal stem cell aging.', *Experimental gerontology*, 40(12), pp. 926–930. doi: 10.1016/j.exger.2005.07.006.
- Ferrera, D. *et al.* (2014) 'Lamin B1 overexpression increases nuclear rigidity in autosomal dominant leukodystrophy fibroblasts', *The FASEB Journal*, 28(9), pp. 3906–3918. doi: 10.1096/fj.13-247635.
- Frantz, C., Stewart, K. M. and Weaver, V. M. (2010) 'The extracellular matrix at a glance', *Journal of Cell Science*, pp. 4195–4200. doi: 10.1242/jcs.023820.
- Friedl, P., Wolf, K. and Lammerding, J. (2011) 'Nuclear mechanics during cell migration', *Current Opinion in Cell Biology*, 23(1), pp. 55–64. doi: 10.1016/j.ceb.2010.10.015.

- Gaggioli, C. *et al.* (2007) 'Fibroblast-led collective invasion of carcinoma cells with differing roles for RhoGTPases in leading and following cells.', *Nature cell biology*, 9(12), pp. 1392–400. doi: 10.1038/ncb1658.
- Ghosh, D. *et al.* (2014) 'Integral role of platelet-derived growth factor in mediating transforming growth factor- β 1-dependent mesenchymal stem cell stiffening.', *Stem cells and development*, 23(3), pp. 245–261. doi: 10.1089/scd.2013.0240.
- Gruenbaum, Y. and Foisner, R. (2015) 'Lamins: Nuclear Intermediate Filament Proteins with Fundamental Functions in Nuclear Mechanics and Genome Regulation', *Annual Review of Biochemistry*. Annual Reviews, 84(1), pp. 131–164. doi: 10.1146/annurev-biochem-060614-034115.
- Haeger, A. *et al.* (2014) 'Cell jamming: Collective invasion of mesenchymal tumor cells imposed by tissue confinement', *Biochimica et Biophysica Acta - General Subjects*. Elsevier B.V., 1840(8), pp. 2386–2395. doi: 10.1016/j.bbagen.2014.03.020.
- Harada, T. *et al.* (2014) 'Nuclear lamin stiffness is a barrier to 3D migration, but softness can limit survival.', *The Journal of cell biology*. The Rockefeller University Press, 204(5), pp. 669–82. doi: 10.1083/jcb.201308029.
- Ho, I. a W. *et al.* (2013) 'Human bone marrow-derived mesenchymal stem cells suppress human glioma growth through inhibition of angiogenesis.', *Stem cells (Dayton, Ohio)*, 31(1), pp. 146–55. doi: 10.1002/stem.1247.
- Hou, Y. *et al.* (2018) 'TASI: A software tool for spatial-temporal quantification of tumor spheroid dynamics', *Scientific Reports*. Nature Publishing Group, 8(1), p. 7248. doi: 10.1038/s41598-018-25337-4.
- Kadota, T. *et al.* (2018) 'Emerging role of extracellular vesicles as a senescence-associated secretory phenotype: Insights into the pathophysiology of lung diseases', *Molecular Aspects of Medicine*. Pergamon, 60, pp. 92–103. doi: 10.1016/J.MAM.2017.11.005.
- Kalluri, R. and Zeisberg, M. (2006) 'Fibroblasts in cancer.', *Nature reviews. Cancer*, 6(5), pp. 392–401. doi: 10.1038/nrc1877.
- Karnoub, A. E. *et al.* (2007) 'Mesenchymal stem cells within tumour stroma promote breast cancer metastasis', *Nature*. Nature Publishing Group, 449(7162), pp. 557–563. doi: 10.1038/nature06188.
- Kasper, G. *et al.* (2009) 'Insights into mesenchymal stem cell aging: involvement of antioxidant defense and actin cytoskeleton.', *Stem cells (Dayton, Ohio)*, 27(6), pp. 1288–1297. doi: 10.1002/stem.49.

- Kim, G.-E. *et al.* (2017) 'Epithelial periostin expression is correlated with poor survival in patients with invasive breast carcinoma', *PLOS ONE*. Edited by A. Ahmad. Public Library of Science, 12(11), p. e0187635. doi: 10.1371/journal.pone.0187635.
- Kole, T. P. *et al.* (2005) 'Intracellular mechanics of migrating fibroblasts', *Biophysical Journal*, 16(January), pp. 328–338. doi: 10.1091/mbc.E04.
- Krtolica, A. *et al.* (2001) 'Senescent fibroblasts promote epithelial cell growth and tumorigenesis: a link between cancer and aging.', *Proceedings of the National Academy of Sciences of the United States of America*, 98(21), pp. 12072–12077. doi: 10.1073/pnas.211053698.
- Kümper, S. and Marshall, C. J. (2011) 'ROCK-driven actomyosin contractility induces tissue stiffness and tumor growth.', *Cancer cell*, 19(6), pp. 695–697. doi: 10.1016/j.ccr.2011.05.021.
- Lacerda, L. *et al.* (2015) 'Mesenchymal stem cells mediate the clinical phenotype of inflammatory breast cancer in a preclinical model', *Breast Cancer Research*, 17(1), p. 42. doi: 10.1186/s13058-015-0549-4.
- Lee, S. and Kumar, S. (2016) 'Actomyosin stress fiber mechanosensing in 2D and 3D', *F1000Research*, 5(0), p. 2261. doi: 10.12688/f1000research.8800.1.
- Lehmann, B. D. *et al.* (2008) 'Senescence-Associated Exosome Release from Human Prostate Cancer Cells', *Cancer Research*, 68(19), pp. 7864–7871. doi: 10.1158/0008-5472.CAN-07-6538.
- Lele, T. P., Dickinson, R. B. and Gundersen, G. G. (2018) 'Mechanical principles of nuclear shaping and positioning', *The Journal of cell biology*. NLM (Medline), pp. 3330–3342. doi: 10.1083/jcb.201804052.
- Levental, K. R. *et al.* (2009) 'Matrix crosslinking forces tumor progression by enhancing integrin signaling.', *Cell*. Elsevier Ltd, 139(5), pp. 891–906. doi: 10.1016/j.cell.2009.10.027.
- Liu, D. and Hornsby, P. J. (2007) 'Senescent Human Fibroblasts Increase the Early Growth of Xenograft Tumors via Matrix Metalloproteinase Secretion', *Cancer Research*, 67(7), pp. 3117–3126. doi: 10.1158/0008-5472.CAN-06-3452.
- Lunyak, V. V, Amaro-Ortiz, A. and Gaur, M. (2017) 'Mesenchymal Stem Cells Secretory Responses: Senescence Messaging Secretome and Immunomodulation Perspective.', *Frontiers in genetics*. Frontiers Media SA, 8, p. 220. doi: 10.3389/fgene.2017.00220.
- Luo, H. *et al.* (2015) 'Cancer-associated fibroblasts: A multifaceted driver of breast cancer progression', *Cancer Letters*, pp. 155–163. doi: 10.1016/j.canlet.2015.02.018.

- Marthandan, S. *et al.* (2016) 'Conserved genes and pathways in primary human fibroblast strains undergoing replicative and radiation induced senescence', *Biological Research*, 49(1), p. 34. doi: 10.1186/s40659-016-0095-2.
- Mathon, N. F. and Lloyd, A. C. (2001) 'Cell senescence and cancer.', *Nature reviews. Cancer*, 1(3), pp. 203–213. doi: 10.1038/35106045.
- McAndrews, K. M., Yi, J., *et al.* (2015) 'Enhanced Adhesion of Stromal Cells to Invasive Cancer Cells Regulated by Cadherin 11', *ACS Chemical Biology*, 10(8), pp. 1932–1938. doi: 10.1021/acscchembio.5b00353.
- McAndrews, K. M., McGrail, D. J., *et al.* (2015) 'Mesenchymal Stem Cells Induce Directional Migration of Invasive Breast Cancer Cells through TGF- β .', *Scientific reports*. Nature Publishing Group, 5, p. 16941. doi: 10.1038/srep16941.
- McGrail, D. J. *et al.* (2012) 'Differential mechanical response of mesenchymal stem cells and fibroblasts to tumor-secreted soluble factors', *PLoS ONE*, 7(3), pp. e33248–e33248. doi: 10.1371/journal.pone.0033248.
- McGrail, D. J. *et al.* (2015) 'SNAIL-induced epithelial-to-mesenchymal transition produces concerted biophysical changes from altered cytoskeletal gene expression', *FASEB Journal*, 29(4), pp. 1280–1289. doi: 10.1096/fj.14-257345.
- McGrail, D. J., McAndrews, K. M. and Dawson, M. R. (2013) 'Biomechanical analysis predicts decreased human mesenchymal stem cell function before molecular differences', *Experimental Cell Research*. Elsevier, 319(5), pp. 684–696. doi: 10.1016/j.yexcr.2012.11.017.
- McLean, K. *et al.* (2011) 'Human ovarian carcinoma-associated mesenchymal stem cells regulate cancer stem cells and tumorigenesis via altered BMP production', *Journal of Clinical Investigation*, 121(8), pp. 3206–3219. doi: 10.1172/JCI45273.
- Mishra, P. J. *et al.* (2008) 'Carcinoma-Associated Fibroblast-Like Differentiation of Human Mesenchymal Stem Cells', *Cancer Research*, 68(11), pp. 4331–4339. doi: 10.1158/0008-5472.CAN-08-0943.
- Muñoz-Espín, D. and Serrano, M. (2014) 'Cellular senescence: from physiology to pathology.', *Nature reviews. Molecular cell biology*. Nature Publishing Group, 15(7), pp. 482–96. doi: 10.1038/nrm3823.
- O'Malley, G. *et al.* (2016) 'Mesenchymal stromal cells (MSCs) and colorectal cancer: a troublesome twosome for the anti-tumour immune response?', *Oncotarget*, 7(37), pp. 60752–60774. doi: 10.18632/oncotarget.11354.

- Orimo, A. *et al.* (2005) 'Stromal fibroblasts present in invasive human breast carcinomas promote tumor growth and angiogenesis through elevated SDF-1/CXCL12 secretion.', *Cell*, 121(3), pp. 335–348. doi: 10.1016/j.cell.2005.02.034.
- Ortiz-Montero, P., Londoño-Vallejo, A. and Vernet, J.-P. (2017) 'Senescence-associated IL-6 and IL-8 cytokines induce a self- and cross-reinforced senescence/inflammatory milieu strengthening tumorigenic capabilities in the MCF-7 breast cancer cell line', *Cell Communication and Signaling*, 15(1), p. 17. doi: 10.1186/s12964-017-0172-3.
- Oswald, L. *et al.* (2017) 'Jamming transitions in cancer', *Journal of Physics D: Applied Physics*. IOP Publishing, 50(48), p. 483001. doi: 10.1088/1361-6463/aa8e83.
- Parrinello, S. *et al.* (2005) 'Stromal-epithelial interactions in aging and cancer: senescent fibroblasts alter epithelial cell differentiation', *Journal of Cell Science*, 118(3).
- Paszek, M. J. *et al.* (2005) 'Tensional homeostasis and the malignant phenotype.', *Cancer cell*, 8(3), pp. 241–254. doi: 10.1016/j.ccr.2005.08.010.
- Perentes, J. Y. *et al.* (2009) 'In vivo imaging of extracellular matrix remodeling by tumor-associated fibroblasts', *Nature Methods*, 6, pp. 2008–2010. doi: 10.1038/NMETH.1295.
- Phillip, J. M. *et al.* (2015) 'The Mechanobiology of Aging', *Annual Review of Biomedical Engineering*. Annual Reviews , 17(1), pp. 113–141. doi: 10.1146/annurev-bioeng-071114-040829.
- Ratajczak-Wielgomas, K. *et al.* (2016) 'Periostin expression in cancer-associated fibroblasts of invasive ductal breast carcinoma', *Oncology Reports*, 36(5), pp. 2745–2754. doi: 10.3892/or.2016.5095.
- Ratajczak-Wielgomas, K. *et al.* (2017) 'Expression of periostin in breast cancer cells', *International Journal of Oncology*, 51(4), pp. 1300–1310. doi: 10.3892/ijo.2017.4109.
- Rodier, F. and Campisi, J. (2011) *Four faces of cellular senescence*, *Journal of Cell Biology*. doi: 10.1083/jcb.201009094.
- Severino, V. *et al.* (2013) 'Insulin-like growth factor binding proteins 4 and 7 released by senescent cells promote premature senescence in mesenchymal stem cells.', *Cell death & disease*. Nature Publishing Group, 4(11), p. e911. doi: 10.1038/cddis.2013.445.
- Shangguan, L. *et al.* (2012) 'Inhibition of TGF- β /Smad Signaling by BAMBI Blocks Differentiation of Human Mesenchymal Stem Cells to Carcinoma-Associated Fibroblasts and Abolishes their Protumor Effects', *STEM CELLS*. Wiley-Blackwell, 30(12), pp. 2810–2819. doi: 10.1002/stem.1251.

Stearns-Reider, K. M. *et al.* (2017) 'Aging of the skeletal muscle extracellular matrix drives a stem cell fibrogenic conversion', *Aging Cell*. John Wiley & Sons, Ltd (10.1111), 16(3), pp. 518–528. doi: 10.1111/accel.12578.

Stephens, A. D. *et al.* (2017) 'Chromatin and lamin A determine two different mechanical response regimes of the cell nucleus', *Molecular Biology of the Cell*. Edited by D. Alex R., 28(14), pp. 1984–1996. doi: 10.1091/mbc.e16-09-0653.

Studený, M. *et al.* (2002) 'Bone marrow-derived mesenchymal stem cells as vehicles for interferon-beta delivery into tumors.', *Cancer research*, 62(13), pp. 3603–3608.

Swanson, E. C. *et al.* (2015) 'Unfolding the story of chromatin organization in senescent cells', *Nucleus*, 6(4), pp. 254–260. doi: 10.1080/19491034.2015.1057670.

Swift, J. *et al.* (2013) 'Nuclear Lamin-A Scales with Tissue Stiffness and Enhances Matrix-Directed Differentiation', *Science*, 341(6149). doi: 10.1126/science.1240104.

Tao, L. *et al.* (2017) 'Cancer associated fibroblasts: An essential role in the tumor microenvironment.', *Oncology letters*. Spandidos Publications, 14(3), pp. 2611–2620. doi: 10.3892/ol.2017.6497.

Theocharidis, G. *et al.* (2016) 'Type VI Collagen Regulates Dermal Matrix Assembly and Fibroblast Motility', *Journal of Investigative Dermatology*. Elsevier, 136(1), pp. 74–83. doi: 10.1038/JID.2015.352.

Tseng, Y., Kole, T. P. and Wirtz, D. (2002) 'Micromechanical mapping of live cells by multiple-particle-tracking microrheology.', *Biophysical Journal*, 83(6), pp. 3162–76. doi: 10.1016/S0006-3495(02)75319-8.

Turinetto, V., Vitale, E. and Giachino, C. (2016) 'Senescence in Human Mesenchymal Stem Cells: Functional Changes and Implications in Stem Cell-Based Therapy.', *International journal of molecular sciences*. Multidisciplinary Digital Publishing Institute (MDPI), 17(7). doi: 10.3390/ijms17071164.

Uccelli, A., Moretta, L. and Pistoia, V. (2008) 'Mesenchymal stem cells in health and disease.', *Nature reviews. Immunology*, 8(9), pp. 726–736. doi: 10.1038/nri2395.

Vallabhaneni, K. C. *et al.* (2016) 'Mesenchymal Stem/Stromal Cells under Stress Increase Osteosarcoma Migration and Apoptosis Resistance via Extracellular Vesicle Mediated Communication', *PLOS ONE*. Edited by G. Camussi. Public Library of Science, 11(11), p. e0166027. doi: 10.1371/journal.pone.0166027.

Wagner, W. *et al.* (2009) 'Aging and replicative senescence have related effects on human stem and progenitor cells.', *PloS one*, 4(6), p. e5846. doi: 10.1371/journal.pone.0005846.

- Wang, N., Tytell, J. D. and Ingber, D. E. (2009) 'Mechanotransduction at a distance: mechanically coupling the extracellular matrix with the nucleus', *Nature Reviews Molecular Cell Biology*. Nature Publishing Group, 10(1), pp. 75–82. doi: 10.1038/nrm2594.
- Wolf, K. *et al.* (2003) 'Compensation mechanism in tumor cell migration: Mesenchymal-amoeboid transition after blocking of pericellular proteolysis', *Journal of Cell Biology*, 160(2), pp. 267–277. doi: 10.1083/jcb.200209006.
- Wolf, K. *et al.* (2009) 'Collagen-based cell migration models in vitro and in vivo', *Seminars in Cell and Developmental Biology*, 20(8), pp. 931–941. doi: 10.1016/j.semcdb.2009.08.005.
- Wu, P.-H., Gilkes, D. M. and Wirtz, D. (2018) 'The Biophysics of 3D Cell Migration'. doi: 10.1146/annurev-biophys.
- Xuan, B. *et al.* (2018) 'Dysregulation in Actin Cytoskeletal Organization Drives Increased Stiffness and Migratory Persistence in Polyploid Giant Cancer Cells', *Scientific Reports*. Nature Publishing Group, 8(1). doi: 10.1038/s41598-018-29817-5.

Figures

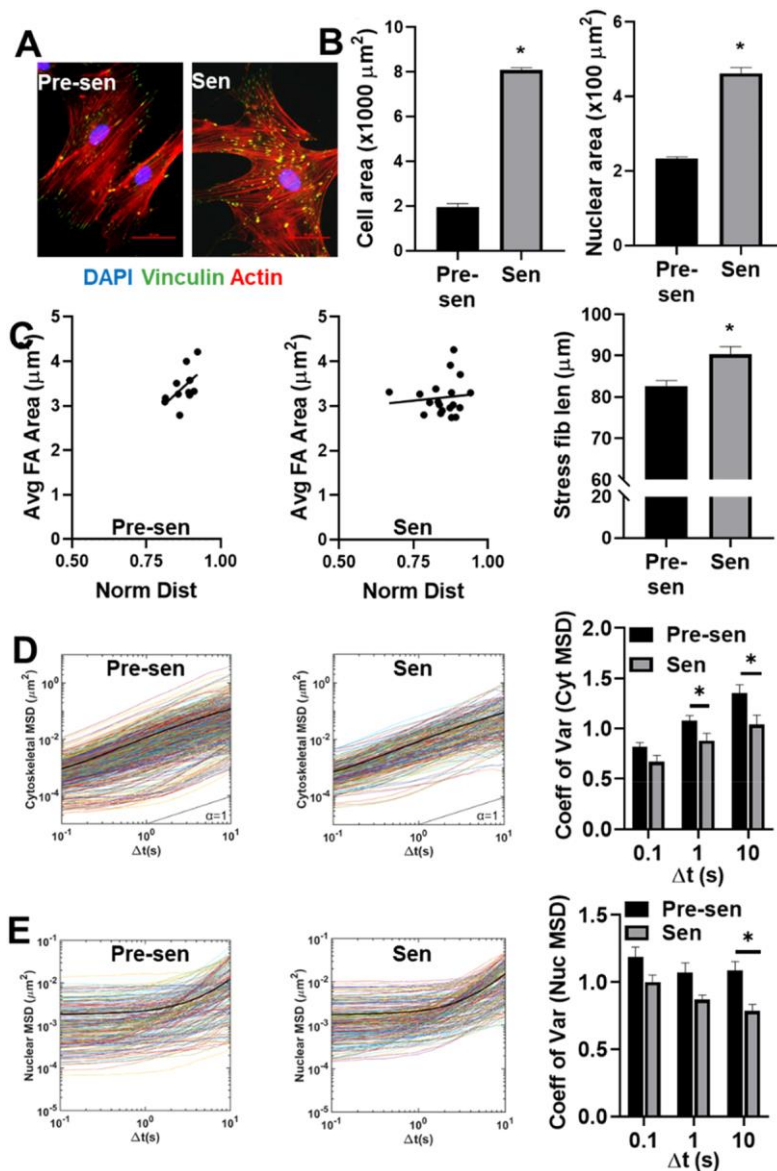


Figure 1: Senescent MSCs displayed altered, cytoskeletal and nuclear organization and mechanics. Human MSCs were treated with 15 Gy γ -irradiation to induce senescence. **(A)** Immunostaining for vinculin (green), actin (red), and DAPI (blue) was used to visualize the actin organization and focal adhesion distribution of MSCs (scale bar=50 μ m). **(B)** Quantification of cell physical parameters revealed senescence induced significant increase in cell and nuclear area. **(C)** Scatter plot of average FA area against the normalized distance of FA from the centroid of the cell demonstrated the altered distribution between pre-senescent and senescent cells. FA size increased more sharply with distance from the centroid in pre-senescent MSCs compared to senescent MSCs. Average stress fiber length increased by ~10% in senescent cells compared to the control. **(D)** Cytoskeletal mechanics was assessed

by tracking the motion of 200-nm probe particles embedded in the cytosol ($n > 15$ cells/condition, $n = 10-20$ particles/cells, $n > 200$ particles/condition). Time-dependent ensemble average MSDs increased linearly with time-scale for both pre-senescent and senescent MSCs; however, MSD distribution were narrower for senescent MSCs. Colored lines represent individual traces from each particle MSDs; whereas, the black line represents the ensemble average MSD of all the particles. Coefficient of variation (CV) were calculated for MSDs at $t = 0.1$, $t = 1$ and $t = 10$ s. Pre-senescent MSCs displayed significantly higher CVs compared to senescent cells at $t = 1$ and $t = 10$ s. **(E)** Nuclear mechanics was assessed by tracking Hoechst-labeled chromatin in the nuclei. At short time-scales the MSDs were independent of time, resembling particle motion in more elastic material; however, at later time scales nuclei transitioned to more viscous behavior indicated by an increasing MSD slope. Colored lines represent traces from each tracked condensed chromatin spot; whereas, the black line represents the ensemble average of all tracks. Coefficients of variation (CV) were calculated for and nuclear MSDs at $t = 0.1$, $t = 1$ and $t = 10$ s. Pre-senescent MSCs displayed significantly higher CVs compared to senescent cells at $t = 10$ s. Student's t-tests were used to calculate statistical significance, and p-values less than 0.05 considered significant (* $p < 0.05$, ** $p < 0.01$, *** $p < 0.001$).

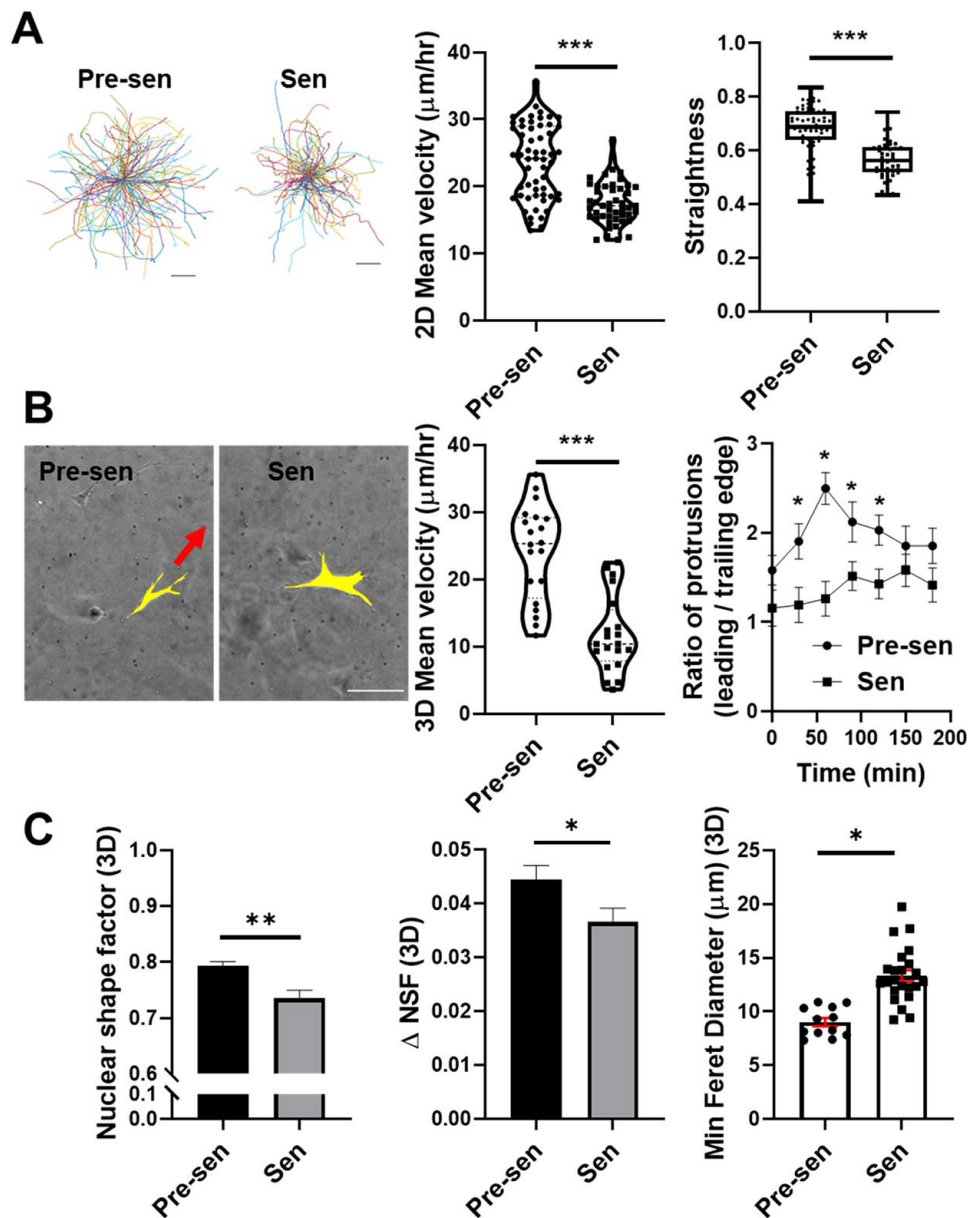
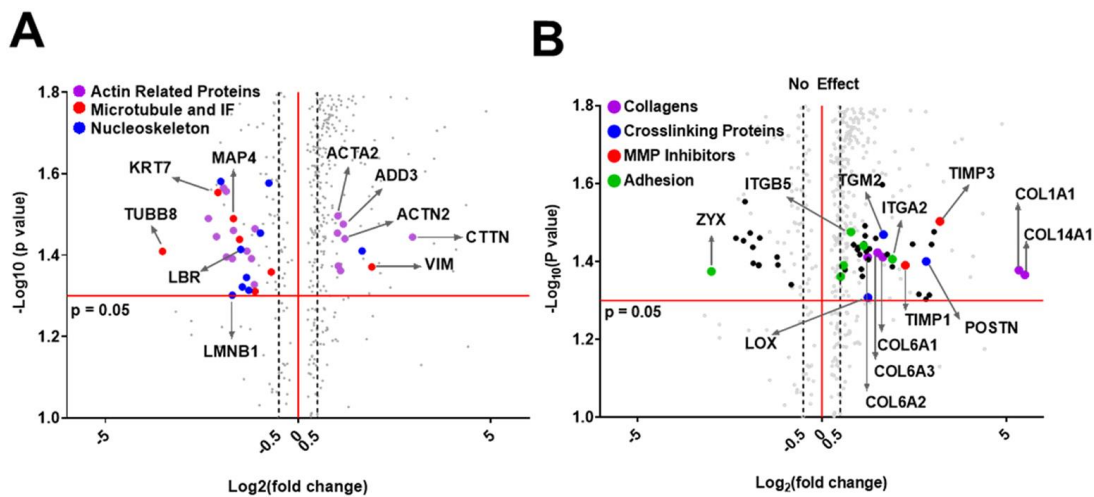


Figure 2: Senescence reduced MSC migration significantly in 2D and 3D. (A) Representative traces of single cell motions and dot plots representing single cell mean velocities, assessed by tracing the motion of Hoechst stained nuclei over 12-hour time period at 10 min intervals. Straightness of cell migration was calculated using total path length over net displacement to assess persistent motion. **(B)** MSCs were embedded in collagen and imaged at 15-minute intervals over 12 hours-time period. Pre-senescent MSCs formed leading edge protrusions in the direction of migration. Whereas, senescent MSCs formed protrusions in multiple directions but were unable to move forward (**scale bar = 100 μm**). Based on nuclear x-y coordinates we tracked hundreds of individual cells for each condition; the mean velocity of senescent MSCs was reduced ($p < 0.001$). For both cell types, leading edge and trailing edge protrusions were counted; we report the ratio of leading to trailing edge protrusions,

which characterizes the likelihood of cells being able to move forward. (C) Nuclear shape factor (NSF), change in NSF(Δ), and minimum ferret diameter were quantified for MSCs in 3D collagen gels. Senescent MSC nuclei were slightly more elongated but less deformable resulting in higher ferret diameters that limited their migration in porous collagen networks. Student's t-tests were used to calculate statistical significance, and p-values less than 0.05 considered significant (* $p < 0.05$, ** $p < 0.01$, *** $p < 0.001$).



● Actin		● Microtubule and IFs	
Protein	log2(FC)	Protein	log2(FC)
CTTN	2.97	VIM	1.91
ACTN2	1.21	KRT19	-0.70
ADD3	1.17	MAPRE1	-1.12
ADD1	1.10	MAP1B	-1.52
CAPN2	1.04	MAP4	-1.68
ACTA2	1.03	KRT7	-2.08
MYO6	1.02	TUBB8	-3.52
ACTL6A	-1.12	IQGAP3	-6.16
TPM3	-1.14	● Nucleoskeleton	
EZR	-1.21	PML	1.66
CNN3	-1.33	MATR3	-0.76
TPM2	-1.68	SUN2	-0.98
MSN	-1.71	TPR	-1.28
DIAPH1	-1.86	IPO11	-1.34
TAGLN2	-1.87	IPO7	-1.45
TAGLN	-1.94	LBR	-1.49
FLNC	-2.12	LMNB1	-1.71
CNN2	-2.33	KPNA7	-2.01

● Collagens		● Other ECM	
Protein	log2(FC)	Protein	log2(FC)
COL12A1	1.13	THBS1	0.63
COL6A2	1.24	FN1	0.86
COL4A2	1.46	TGFBI	1.07
COL6A3	1.51	BGN	1.15
COL5A2	1.64	SPARC	1.17
COL6A1	1.65	LAMC1	1.26
COL1A2	2.46	FBN1	1.29
COL4A1	2.82	LAMB1	2.63
COL1A1	5.34	POSTN	2.83
COL14A1	5.50	VTN	3.04
● Matrix Modifying Enzymes			
TIMP1	2.26	LOX	1.25
MMP2	2.91	TGM2	1.67
TIMP3	3.20	P4HA1	1.77
● Adhesion Molecules			
ZYX	-2.99	ITGBL1	0.79
ITGB1	0.51	ITGB5	1.13
VCL	0.59	ITGA2	1.91

Figure 3: Mass spectrometric analysis of differentially regulated peptides in senescent vs. pre-senescent MSCs. Comprehensive proteomic analysis was performed to find significantly (q value <0.05) changed peptides between the senescent and pre-senescent MSCs ($n=4$). The overall list of pathway specific genes was examined using GO cellular component analysis. Differentially altered proteins are highlighted in gray in volcano plots, and critical genes are color-coded based on function. Log₂ fold changes are also tabulated for key dysregulated genes. **(A)** Proteomic analysis was used to identify Log₂ fold changes in the expression of cytoskeleton and nucleoskeleton related proteins for senescent vs. pre-senescent MSCs, including actin-related proteins (**magenta**), microtubules and intermediate filaments (IFs) (**red**), and nucleoskeleton (**blue**). **(B)** Analysis of ECM related proteins was used to identify Log₂ fold changes in expression of collagens, and other ECM proteins and

crosslinkers for senescent MSCs compared to pre-senescent MSCs. Critical genes for ECM synthesis and turnover are highlighted in the volcano plot, including collagen isoforms (**red**), crosslinking proteins (**blue**), and MMP inhibitors (**green**). It is notable that POSTN, COL1A1, COL14A1, and TIMP3 are among most-highly upregulated proteins.

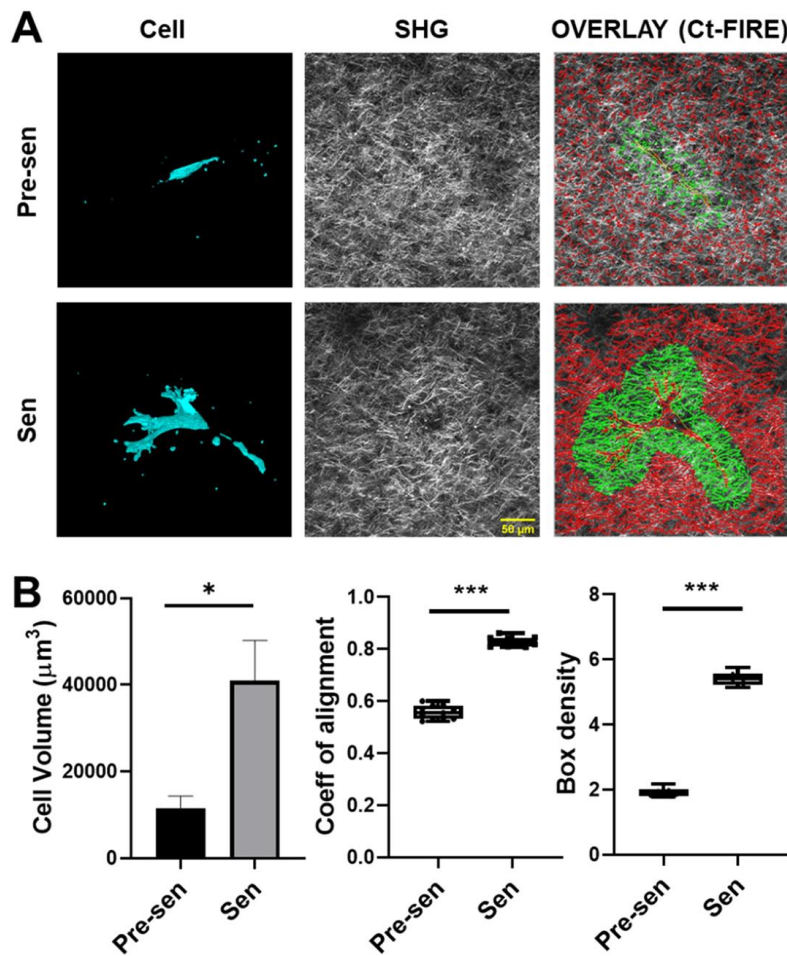


Figure 4: MSC volume and matrix remodeling in 3D collagen gels. MSCs were embedded in collagen gels and incubated for 72hours. Then, the collagen gels were fixed and imaged using multiphoton microscopy for collagen fibers by SHG (cyan) and MSCs (red) using CFSE. (A) A 3D reconstruction of MSCs along with corresponding processed SHG images showing the collagen density heatmap around cells were used to quantify physical parameters of the cells and the surrounding ECM (scale bar = 50 μm). (B) MSC volumes were calculated using Image J voxel counter plugin; whereas, ECM properties surrounding the cells were determined using Ct-Fire. Initially, cell boundaries were traced manually and saved as a mask. Subsequently, uniform dilation of 50 μm around the cell outline was used to determine the local fiber properties surrounding the cells including, coefficient of alignment and density (ROI highlighted in green). Volume of senescent MSCs was significantly larger. Additionally, both fiber alignment and density of the ECM surrounding senescent MSCs were significantly increased. Student's t-tests were used to calculate statistical significance, and p-values less than 0.05 considered significant (* $p < 0.05$, ** $p < 0.01$, *** $p < 0.001$).

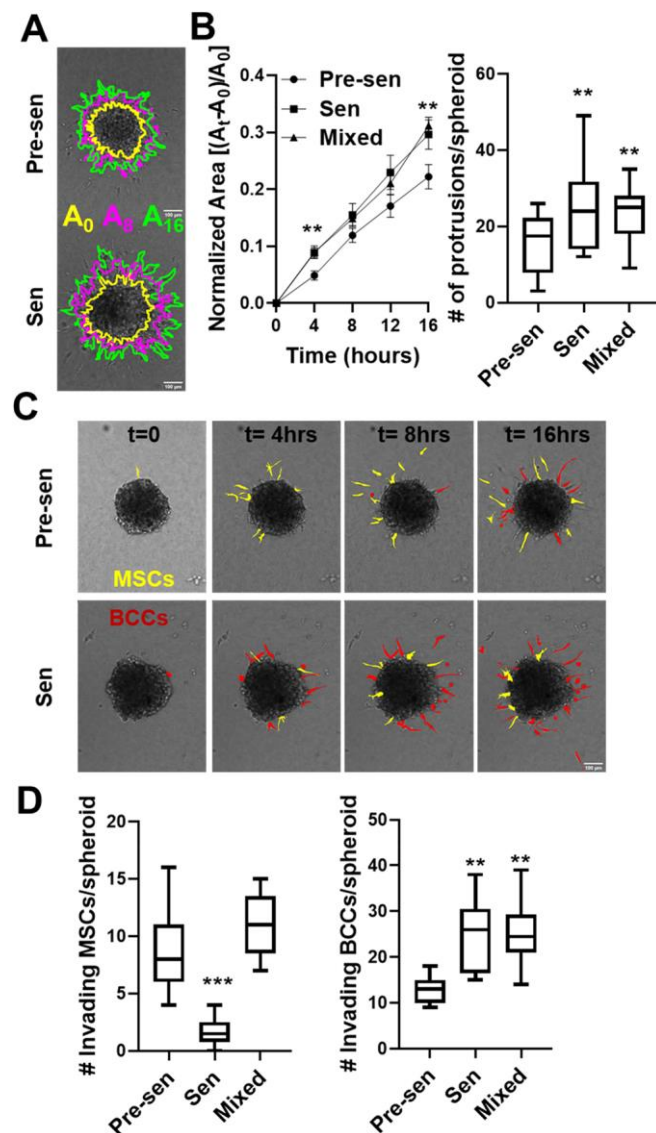


Figure 5: Senescent MSCs promoted BCC invasion in a 3D matrix interface model. (A) Time-lapsed imaging was used to monitor cell migration from spheroids using matrix interface model. Spheroids formed from equal numbers of GFP labeled BCCs and unlabeled MSCs (pre-senescent, senescent, mixed) were monitored over 16hours period at 30-minute intervals. Images of spheroid migration over time with regions highlighted in yellow, magenta and green depict the area at times, t= 0, 8 and 16 hours, respectively (**scale bar = 100 μ m**). **(B)** Spheroid area over time was quantified. We report the change in spheroid area normalized to initial area. The number of protrusions were calculated using Temporal analysis of spheroid imaging (TASI) to assess the invasiveness of spheroids. **(C)** Time-lapsed images of individual cell invasion is highlighted for invading MSCs in **yellow** and cancer cells in **red**. **(D)** We quantified the number of MSCs and BCCs that detached from spheroid surface and were

individually invading the surrounding ECM. Senescent MSCs promoted collective spheroid invasion with increased normalized invaded area and increased number of protrusions as well as individual BCC invasion in collagen. Student's t-tests were used to calculate statistical significance, and p-values less than 0.05 considered significant (* $p < 0.05$, ** $p < 0.01$, *** $p < 0.001$).

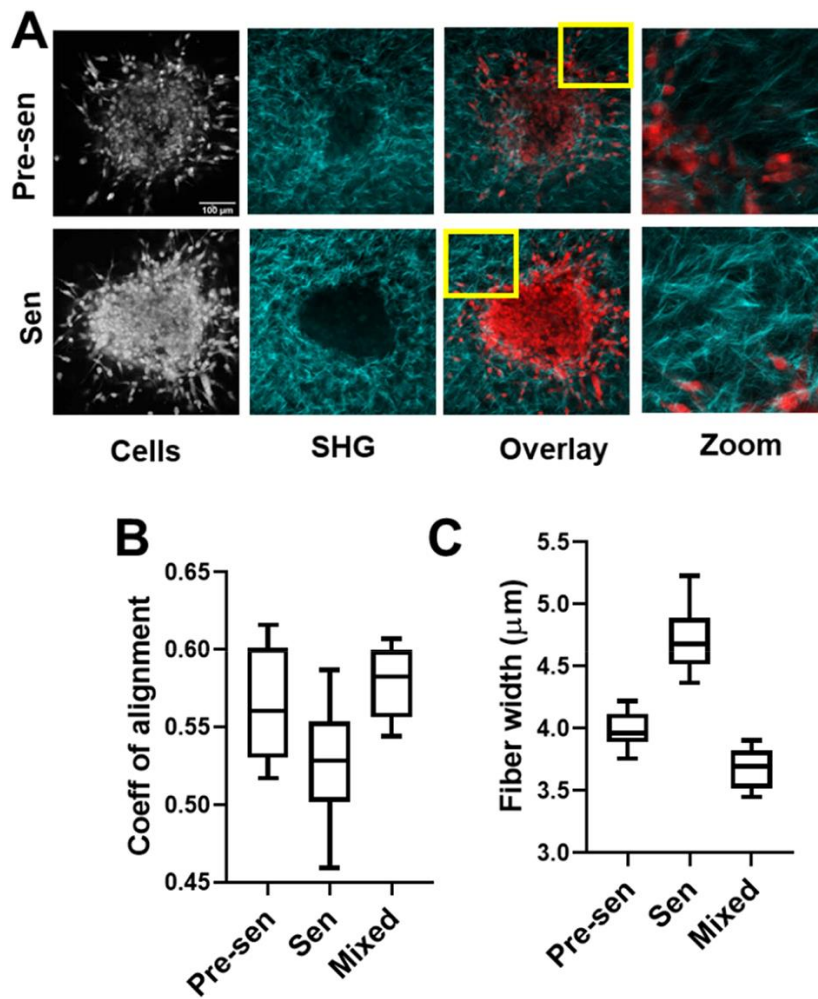


Figure 6: Senescent MSCs rapidly remodeled the extracellular matrix. (A) Spheroids embedded in collagen gels were imaged by multiphoton microscopy using second harmonic generation to identify collagen (shown in **cyan**) and NucRed to identify cells. (C-D) SHG images were analyzed using CurveAlign to quantify collagen fiber properties and orientation. Coefficient of alignment measuring degree of collagen alignment surrounding spheroids was enhanced with pre-senescent cells (C); whereas collagen fiber width was increased for spheroids containing senescent cells only (D). Student's t-tests were used to calculate statistical significance, and p-values less than 0.05 considered significant (* $p < 0.05$, ** $p < 0.01$, *** $p < 0.001$).

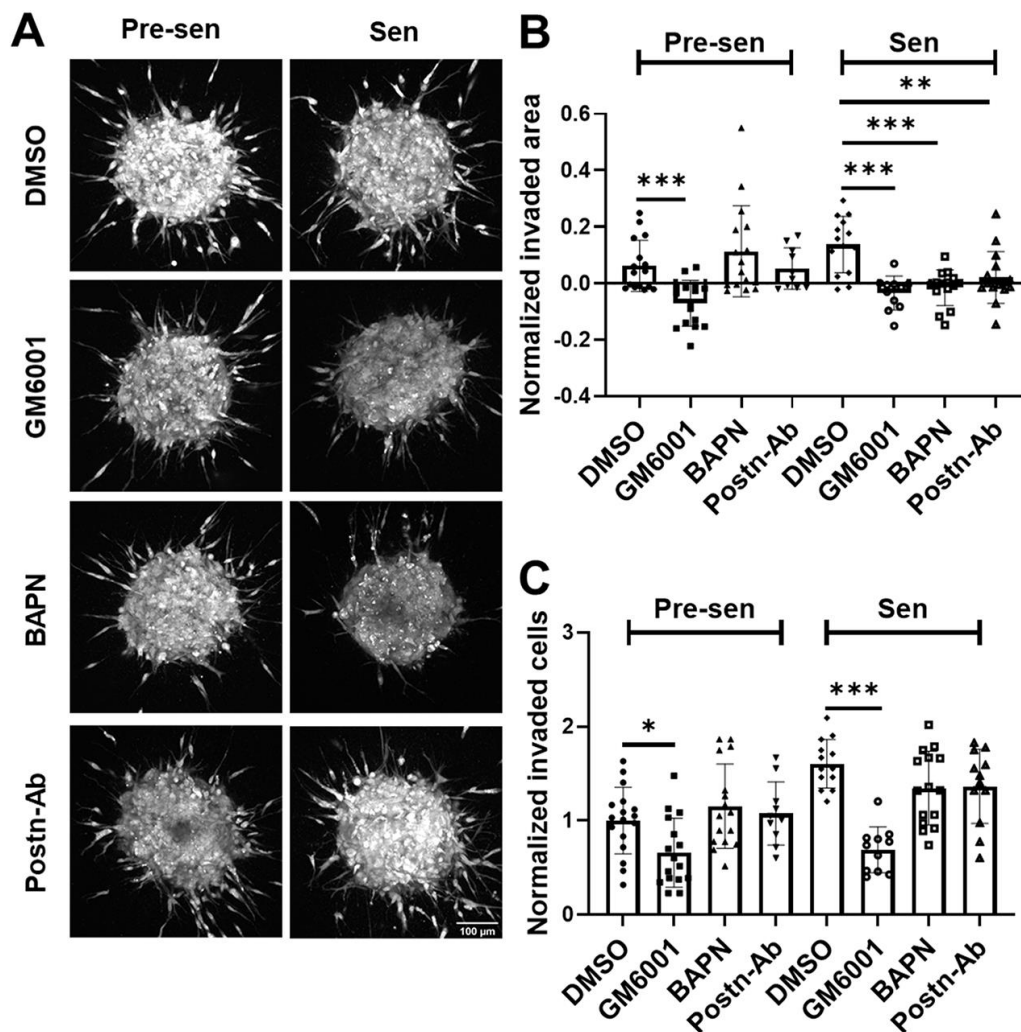


Figure 7: Targeting senescence-associated ECM modifications to reverse invasive BCC phenotype. (A) Time-lapsed imaging was used to monitor invasion over 16 hours from spheroids co-cultured with MDA-MB-231 and MSCs. Spheroids were individually treated with small molecule inhibitors for MMPs (GM6001), and LOX (BAPN), and neutralizing antibody for POSTN (Scale bar= 100 μ m). We quantified (B) the normalized change in invaded area relative to initial area., and (C) number of invading cells respective untreated controls. GM-6001 targeted both pre-senescent and senescent MSC containing spheroids. However, targeting LOX (BAPN) and periostin (Ab) specifically blocked the increased invaded area but not the number of invading cells in case of senescent cell containing spheroids. Student's t-tests were used to calculate statistical significance, and p-values less than 0.05 considered significant (*p < 0.05, **p < 0.01, ***p < 0.001).

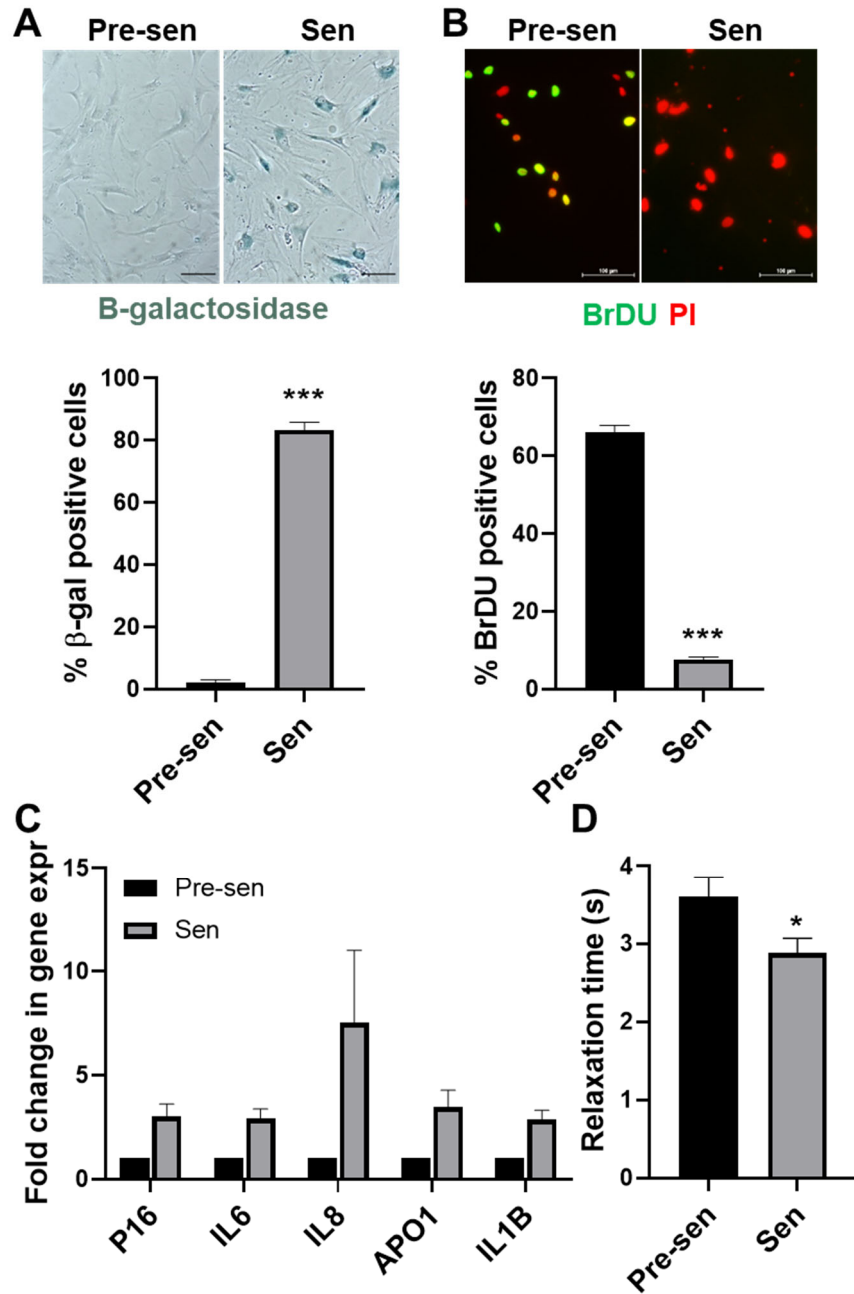


Figure S1. **(A-C) Characterization of radiation induced senescence and development of SASP in MSCs.** Staining and quantification of **(A)** SA- β -galactosidase (blue) and **(B)** BRDU (green: BrDU, red: propidium iodide) incorporation confirmed senescence in irradiated MSCs. **(C)** mRNA expression analysis by qRT-PCR for senescence markers (APO1, P16, IL6, IL8, IL1B); expression of all SASP markers was increased. **(D)** Quantification of average relaxation time (RT) for the nucleus signifying its transition into viscous domain showed significantly lower RT for senescent compared to pre-senescent MSCs. Student's t-tests were used to calculate statistical significance, and p-values less than 0.05 considered significant (* $p < 0.05$, ** $p < 0.01$, *** $p < 0.001$).

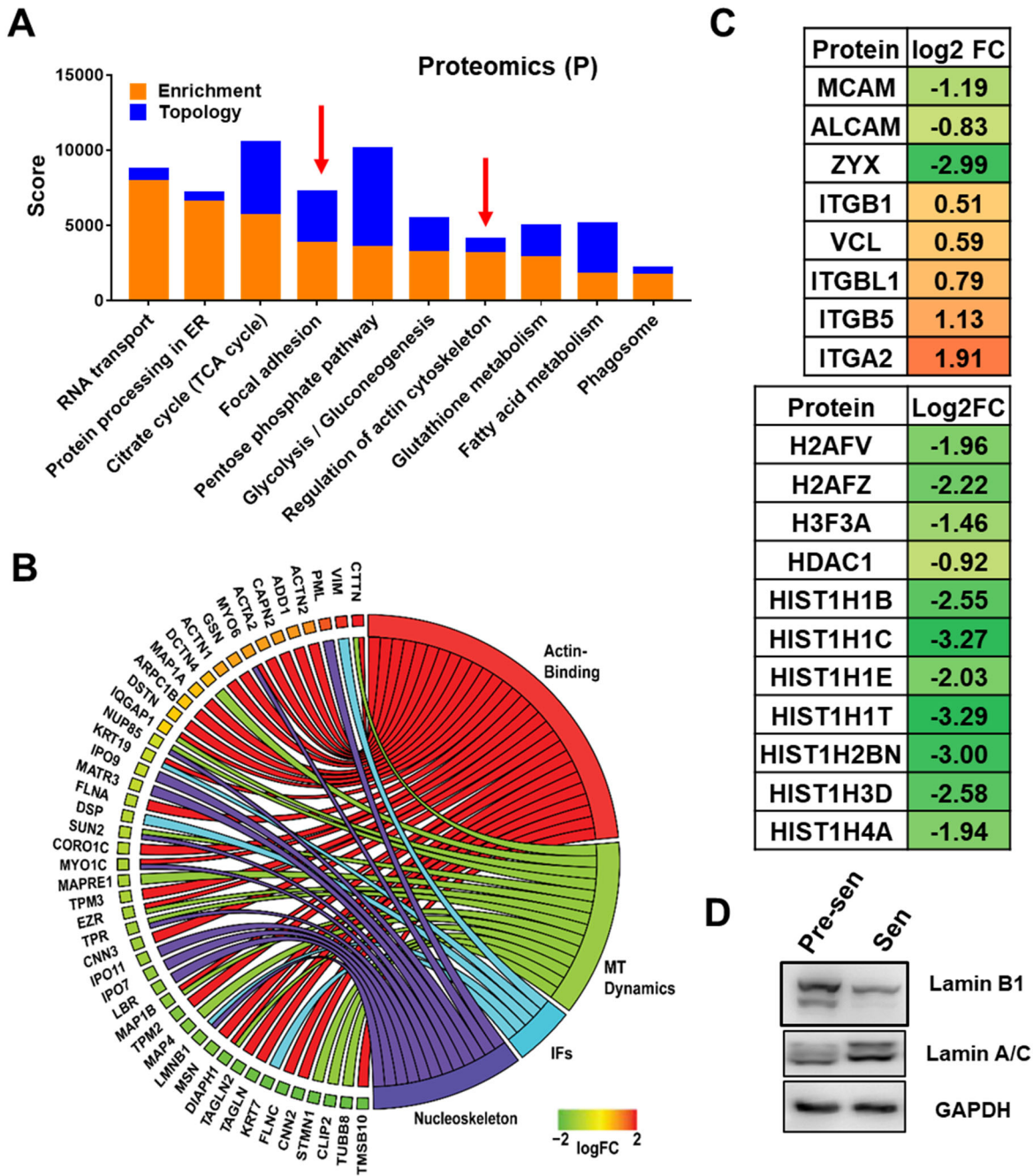


Figure S2. **Pathway analysis of senescence induced changes in protein expression.** (A) Analysis of differentially regulated peptides showed enrichment for pathways including, focal adhesion, and actin cytoskeleton (red arrows). (B) GO chord plot of protein expression for senescent versus pre-senescent MSCs are reported for cytoskeleton and nucleoskeleton related proteins (FC-fold change, MT-Microtubule, IF-Intermediate filament). (C) Log2 FC in expression for genes related to adhesion and histone modification. (D) Western blot was used to analyze expression of LMNA and LMNB1 in senescent MSCs. While LMNA expression was upregulated, LMNB1 was downregulated in senescent MSCs compared to pre-senescent cells.

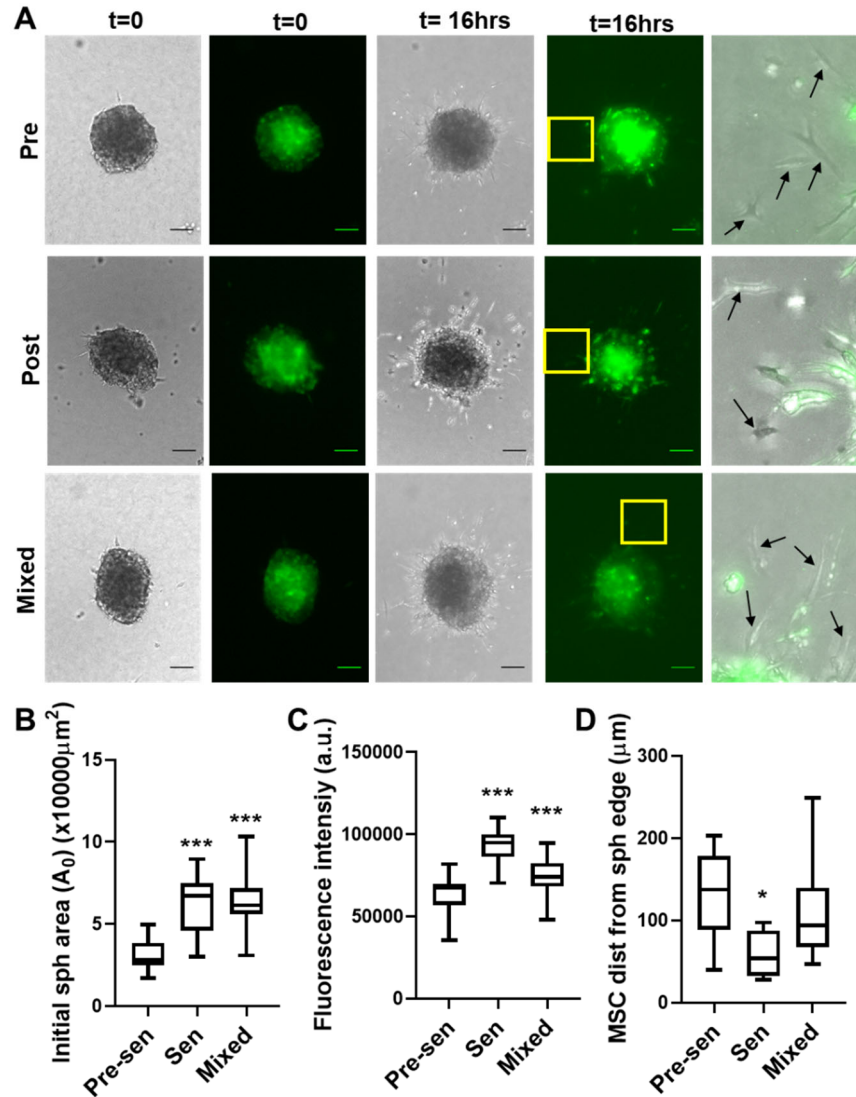


Figure S3. **Comparative role of pre-senescent and senescent MSCs in BCC invasion in 3D collagen gels.** (A) Time-lapsed imaging was used to monitor BCC invasion over 16 hours from spheroids formed with equal numbers of GFP negative MSCs and GFP positive MDA-MB-231 cells and embedded in 1.5 mg/ml collagen gels (Scale bar 100 μm). Pre-senescent and senescent MSCs were also combined at 1:1 ratio (mixed). (B-C) Initial area (A_0) of the embedded spheroids (B) and fluorescence measurement of GFP positive MDA-MB-231 cells (measured with plate reader) (C) were quantified to assess the number of BCCs. Presence of senescent cells resulted in spheroids with larger initial area and higher number of BCCs. (D) To assess the role of MSCs in invasion, we quantified the invaded distance of MSCs from spheroid boundary. This confirms that pre-senescent MSCs move further from spheroid surface than senescent MSCs. Student's t-tests were used to calculate statistical significance, and p-values less than 0.05 considered significant (* $p < 0.05$, ** $p < 0.01$, *** $p < 0.001$).

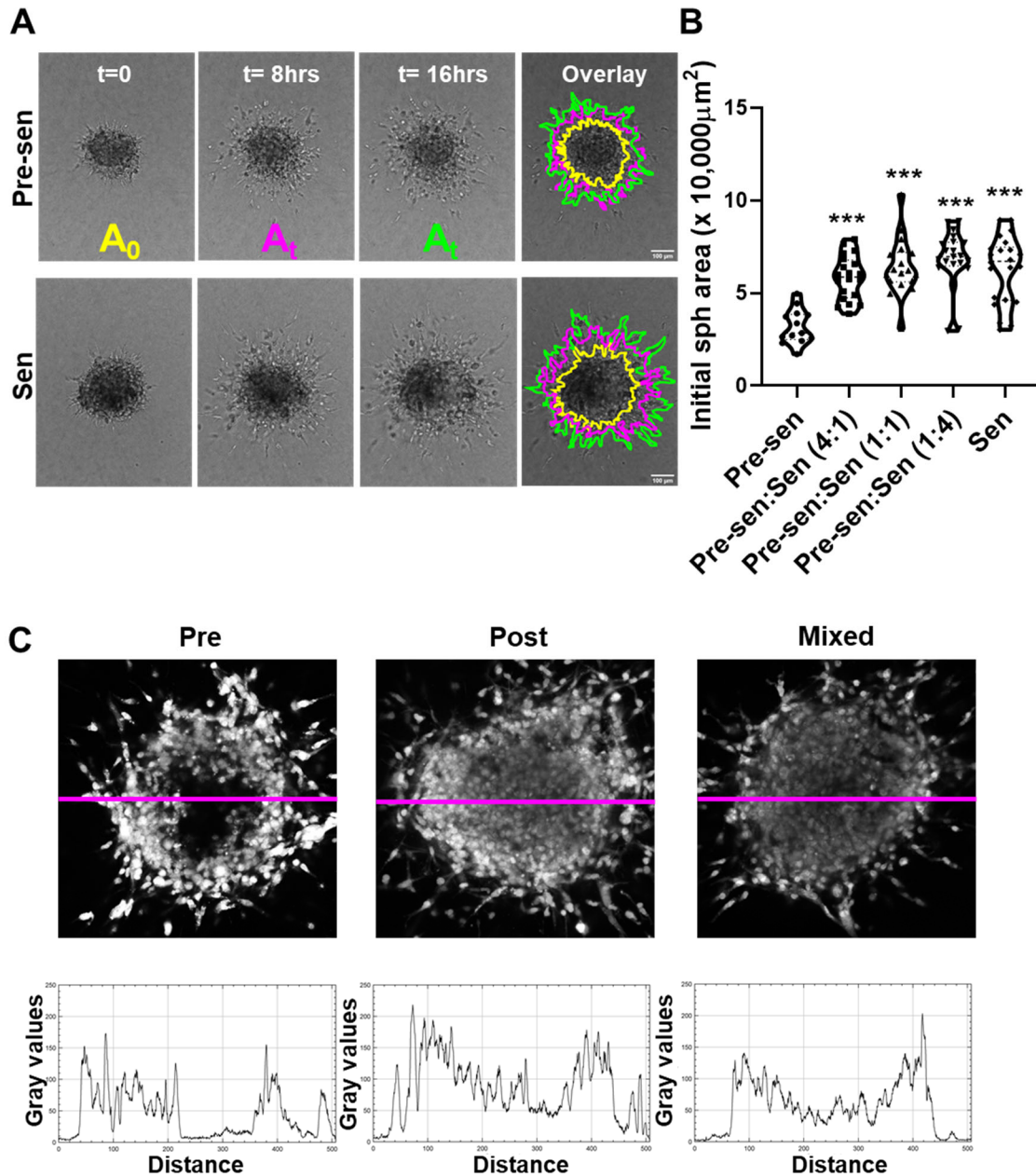


Figure S4. **Role of pre-senescent and senescent MSCs in organization of spheroid and invasion.** (A) Time-lapsed imaging was used to monitor cell migration from spheroids using matrix interface model. Images of spheroid migration over time with regions highlighted in yellow, magenta and green depict the area at times, $t = 0, 8$ and 16 hours, respectively (scale bar = $100 \mu\text{m}$). (B) Spheroid area was analyzed for MDA-MB-231 cell spheroids cultured with both individual and mixed population of pre-senescent and senescent MSCs embedded in collagen gels. For the mixed populations, the ratio between MSCs were varied between 4:1 to 1:4. The presence of senescent MSCs increased spheroid size for all ratios compared to spheroids with only pre-senescent MSCs. (C) Images from multiphoton confocal microscopy were used to determine cell density distribution in 3D spheroids. The gray intensity representing cell distribution across the central axis (magenta) of the spheroid core was plotted in ImageJ to look at differences in cell density at spheroid core.

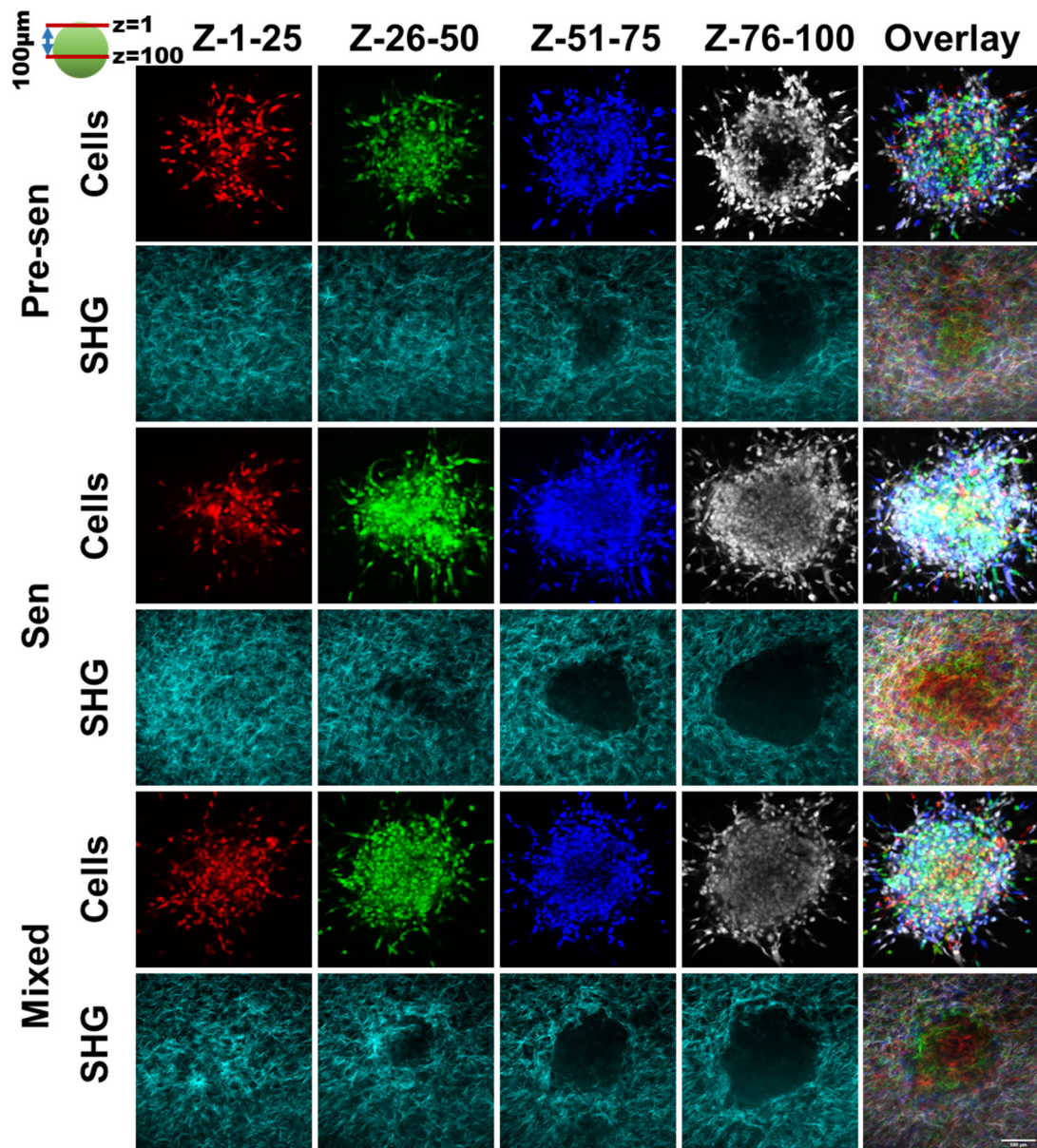


Figure S5. **SHG analysis of collagen structure surrounding spheroids.** Spheroids embedded in collagen gels were imaged by multiphoton microscopy using second harmonic generation to identify collagen (shown in **cyan**) and NucRed to identify cells. Cell z-stacks were color coded (*red: z1-25, green: z26- 50, blue: z51-75, gray: z76-100*) to distinguish different sections of the spheroid (**scale bar=100µm**). Mosaic images (overlay) of the color-coded sections highlight packing density of spheroids, which is increased for spheroids co-cultured with senescent MSCs.

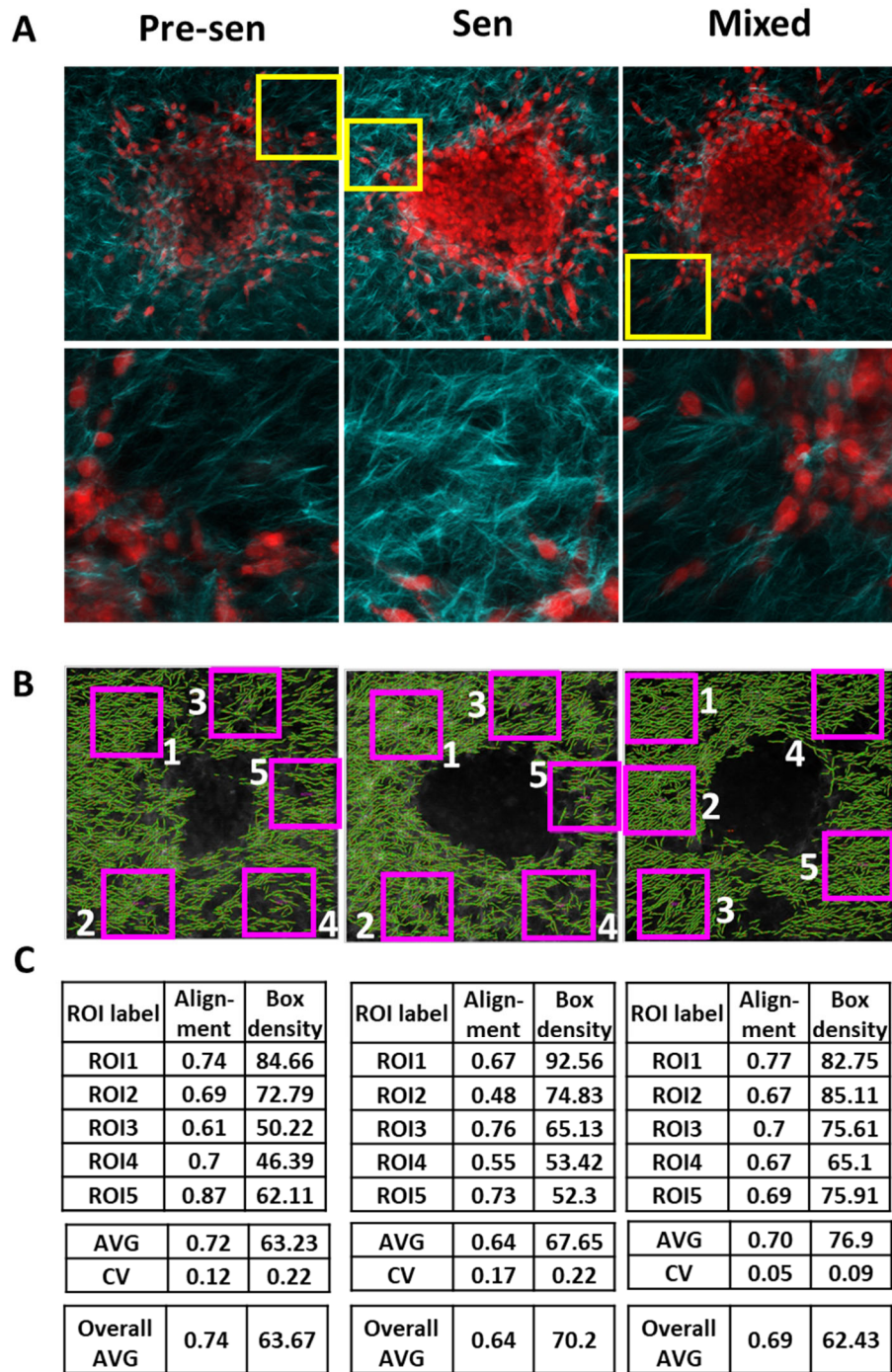


Figure S6. Analysis of local and global structure surrounding spheroids using CT-FIRE. (A) Spheroids embedded in collagen gels were imaged by multiphoton microscopy using second harmonic generation to identify collagen (shown in **cyan**) and NucRed to identify cells (shown in **red**); images include average intensity projections of z-stack and 2D slice for region highlighted by yellow box. (B-C) The structure of collagen around the embedded spheroid was analyzed using CurveAlign ROI analysis. For each image, 5 rectangular boxes were selected around the primary spheroid to quantify co-efficient of alignment. Properties of the ROIs along with the overall image are reported here.

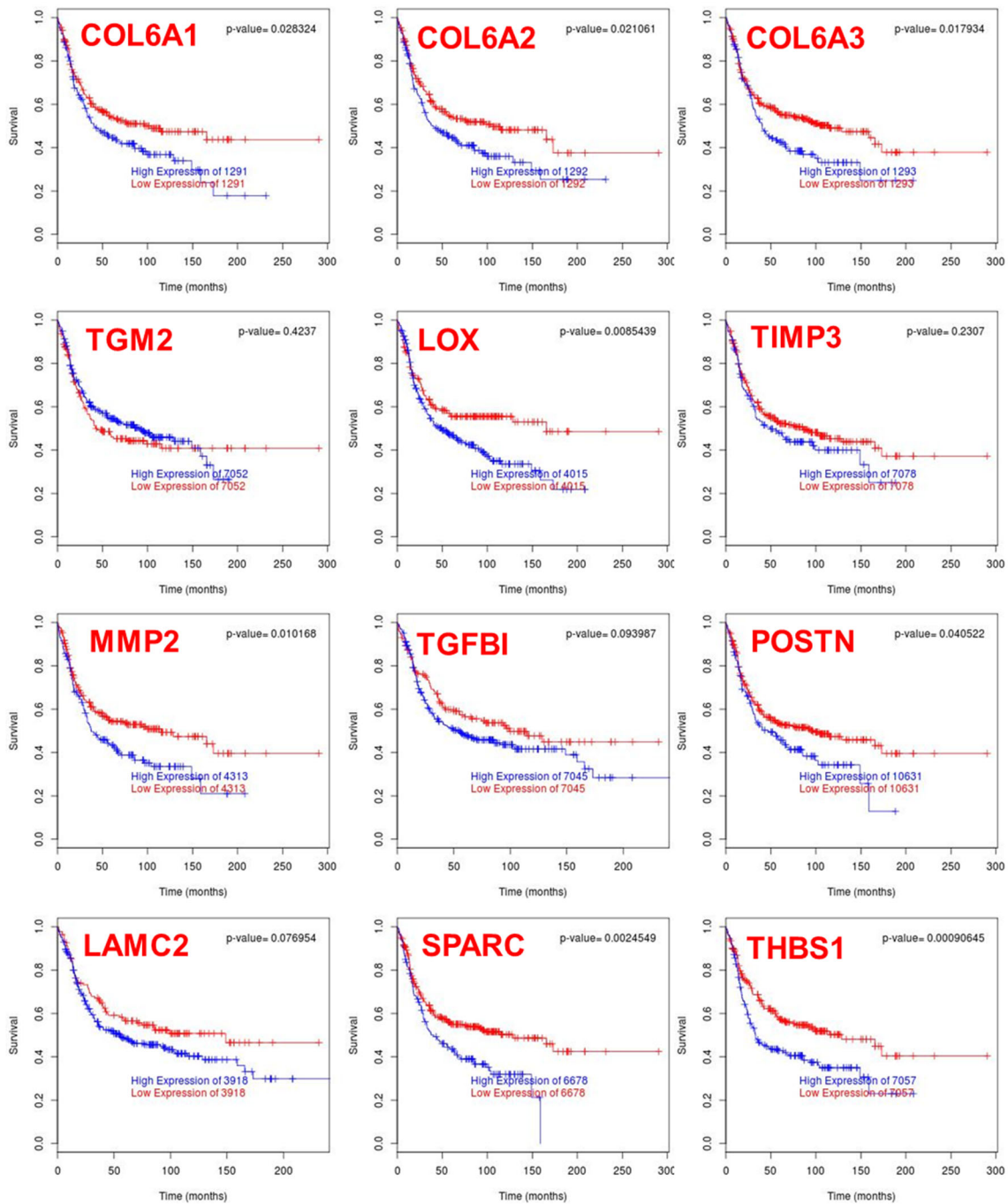


Figure S7. Survival analysis of senescent associated ECM signature in breast cancer. ECM signature from senescent MSCs was used to analyze Kaplan-Meier estimates of disease-free survival for breast cancer using free online tool BreastMark at <http://glados.ucd.ie/BreastMark/index.html>. ECM genes upregulated in senescent MSCs including, expression of collagen isoforms (COL6A1, COL6A2, COL6A3), matrix modifying enzymes (LOX, MMP2), and matricellular proteins (POSTN, THBS1, SPARC) are correlated with poor prognosis in basal subtype of breast cancer ($p < 0.05$).

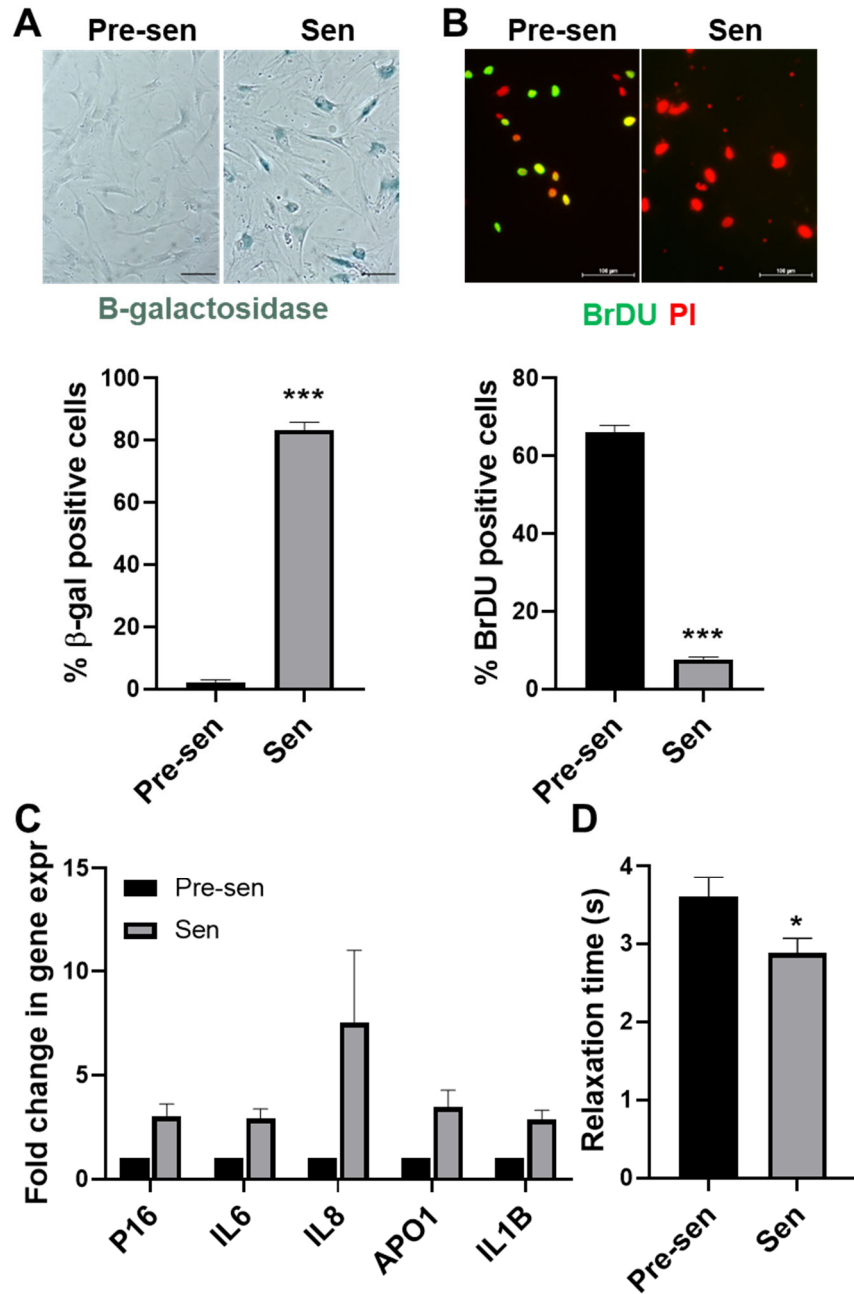


Figure S1. **(A-C) Characterization of radiation induced senescence and development of SASP in MSCs.** Staining and quantification of **(A)** SA- β -galactosidase (blue) and **(B)** BRDU (green: BrDU, red: propidium iodide) incorporation confirmed senescence in irradiated MSCs. **(C)** mRNA expression analysis by qRT-PCR for senescence markers (APO1, P16, IL6, IL8, IL1B); expression of all SASP markers was increased. **(D)** Quantification of average relaxation time (RT) for the nucleus signifying its transition into viscous domain showed significantly lower RT for senescent compared to pre-senescent MSCs. Student's t-tests were used to calculate statistical significance, and p-values less than 0.05 considered significant (* $p < 0.05$, ** $p < 0.01$, *** $p < 0.001$).

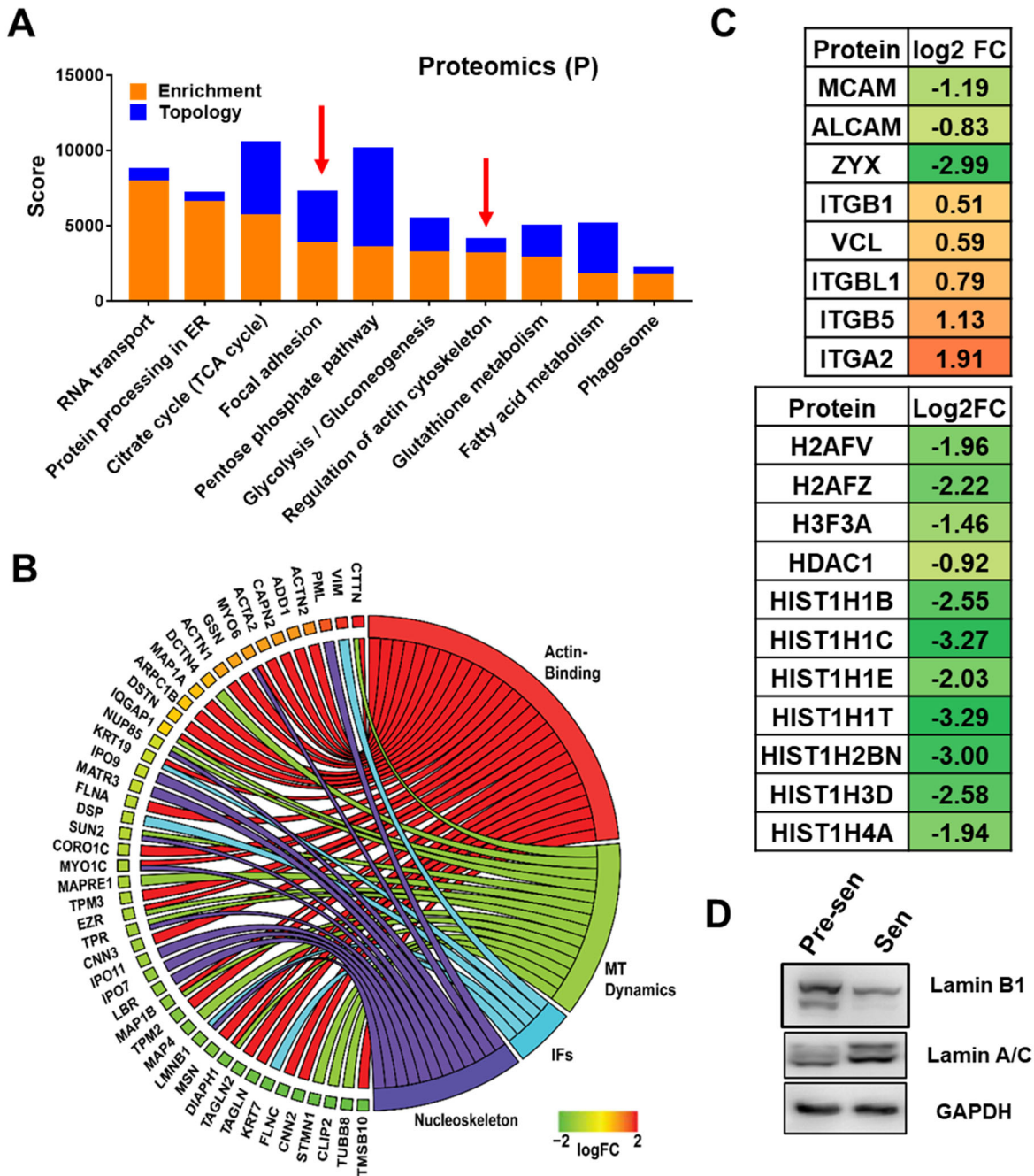


Figure S2. **Pathway analysis of senescence induced changes in protein expression.** (A) Analysis of differentially regulated peptides showed enrichment for pathways including, focal adhesion, and actin cytoskeleton (red arrows). (B) GO chord plot of protein expression for senescent versus pre-senescent MSCs are reported for cytoskeleton and nucleoskeleton related proteins (FC-fold change, MT-Microtubule, IF-Intermediate filament). (C) Log2 FC in expression for genes related to adhesion and histone modification. (D) Western blot was used to analyze expression of LMNA and LMNB1 in senescent MSCs. While LMNA expression was upregulated, LMNB1 was downregulated in senescent MSCs compared to pre-senescent cells.

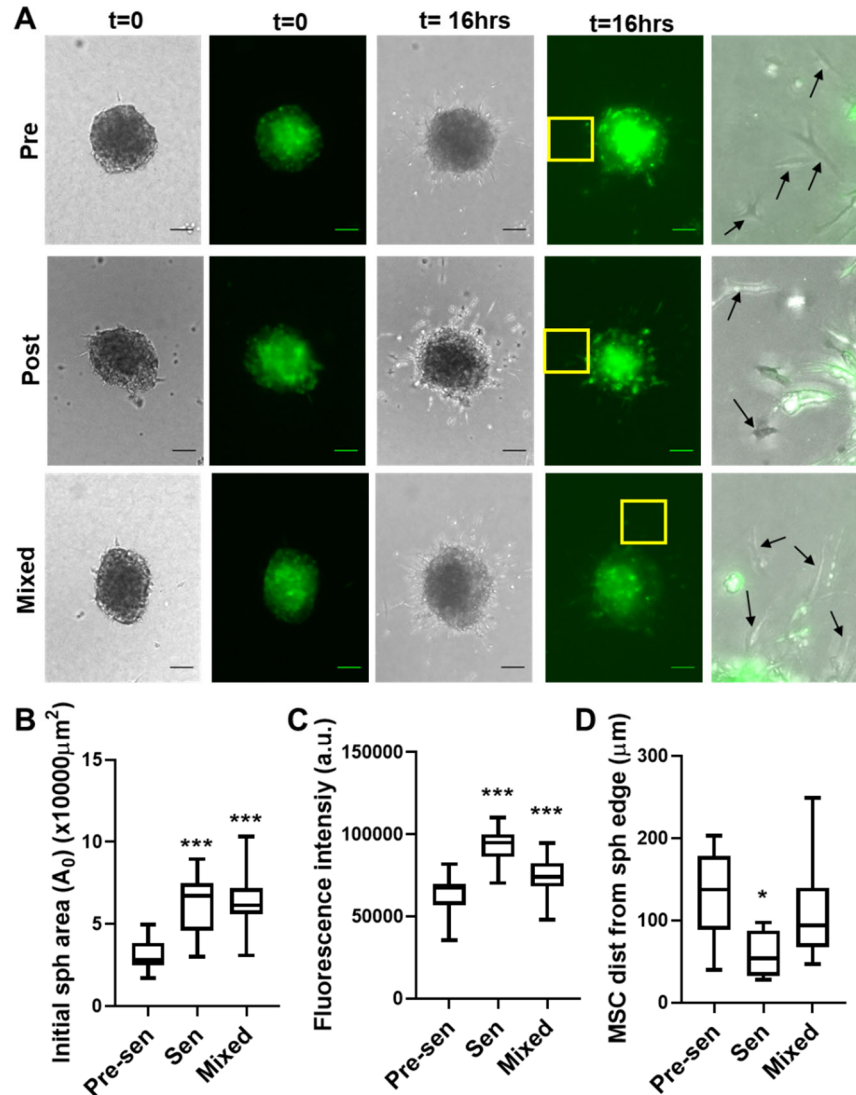


Figure S3. **Comparative role of pre-senescent and senescent MSCs in BCC invasion in 3D collagen gels.** (A) Time-lapsed imaging was used to monitor BCC invasion over 16 hours from spheroids formed with equal numbers of GFP negative MSCs and GFP positive MDA-MB-231 cells and embedded in 1.5 mg/ml collagen gels (Scale bar 100 μm). Pre-senescent and senescent MSCs were also combined at 1:1 ratio (mixed). (B-C) Initial area (A_0) of the embedded spheroids (B) and fluorescence measurement of GFP positive MDA-MB-231 cells (measured with plate reader) (C) were quantified to assess the number of BCCs. Presence of senescent cells resulted in spheroids with larger initial area and higher number of BCCs. (D) To assess the role of MSCs in invasion, we quantified the invaded distance of MSCs from spheroid boundary. This confirms that pre-senescent MSCs move further from spheroid surface than senescent MSCs. Student's t-tests were used to calculate statistical significance, and p-values less than 0.05 considered significant (* $p < 0.05$, ** $p < 0.01$, *** $p < 0.001$).

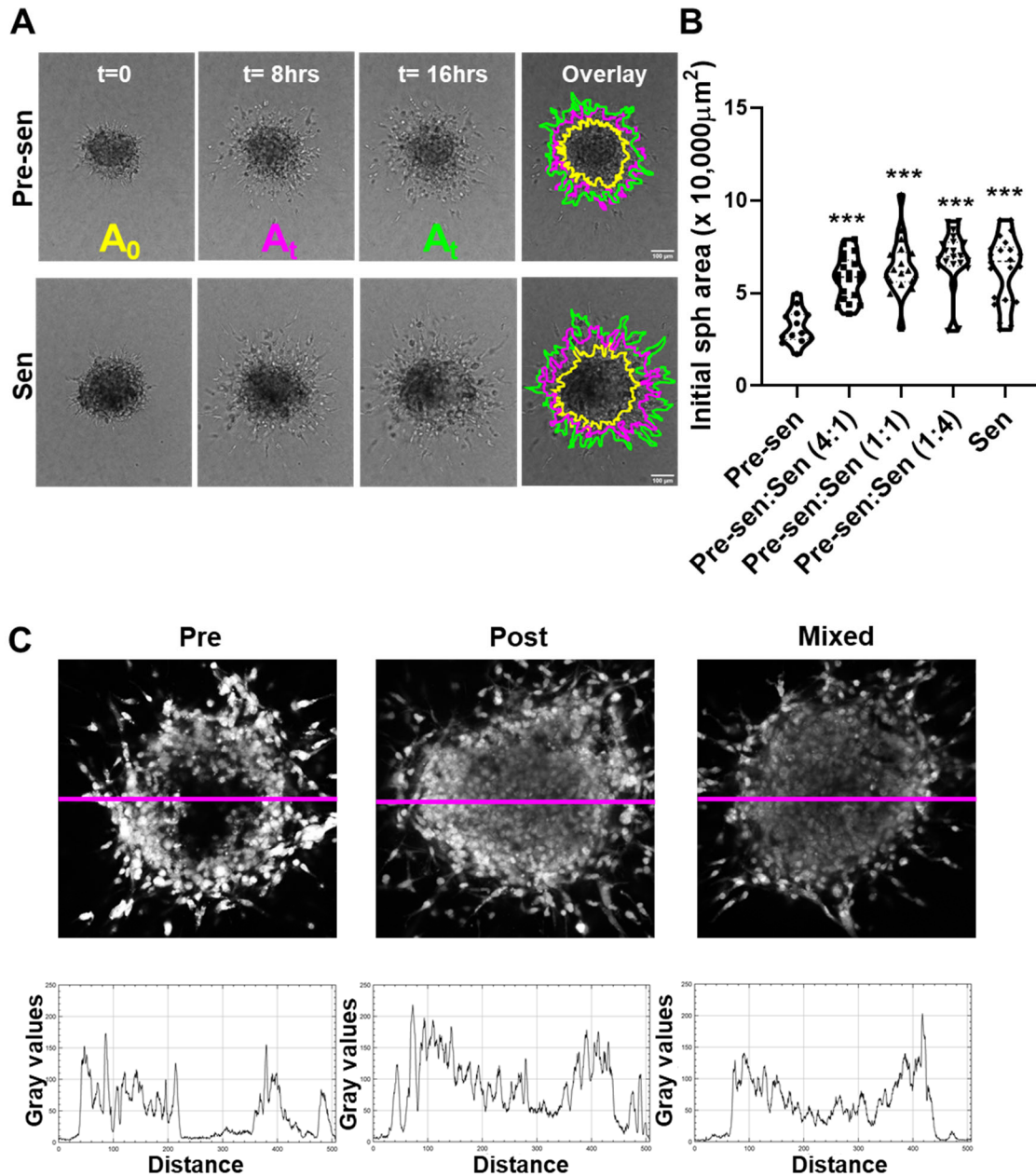


Figure S4. Role of pre-senescent and senescent MSCs in organization of spheroid and invasion. (A) Time-lapsed imaging was used to monitor cell migration from spheroids using matrix interface model. Images of spheroid migration over time with regions highlighted in yellow, magenta and green depict the area at times, $t = 0, 8$ and 16 hours, respectively (scale bar = $100 \mu\text{m}$). (B) Spheroid area was analyzed for MDA-MB-231 cell spheroids cultured with both individual and mixed population of pre-senescent and senescent MSCs embedded in collagen gels. For the mixed populations, the ratio between MSCs were varied between 4:1 to 1:4. The presence of senescent MSCs increased spheroid size for all ratios compared to spheroids with only pre-senescent MSCs. (C) Images from multiphoton confocal microscopy were used to determine cell density distribution in 3D spheroids. The gray intensity representing cell distribution across the central axis (magenta) of the spheroid core was plotted in ImageJ to look at differences in cell density at spheroid core.

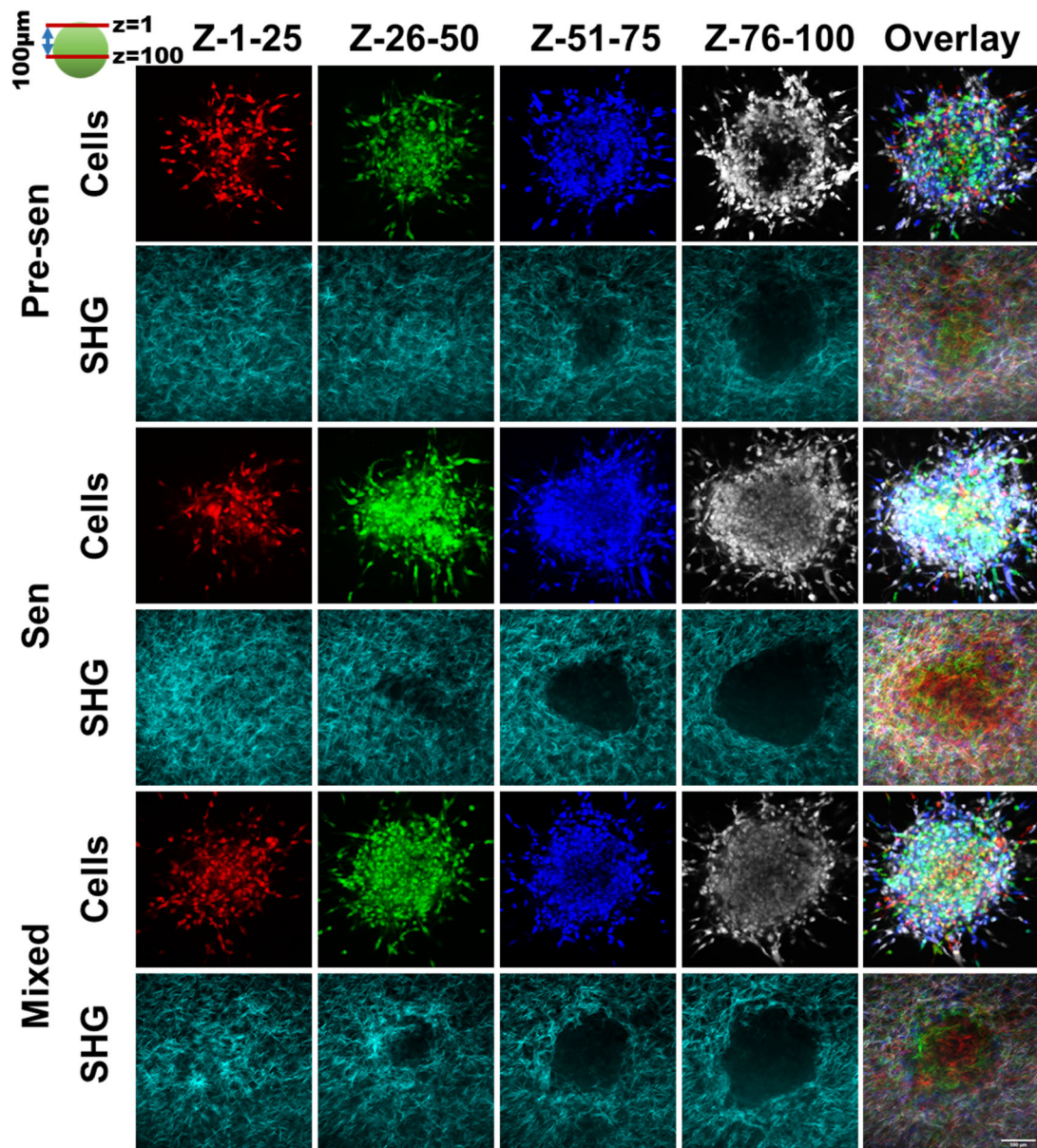


Figure S5. **SHG analysis of collagen structure surrounding spheroids.** Spheroids embedded in collagen gels were imaged by multiphoton microscopy using second harmonic generation to identify collagen (shown in **cyan**) and NucRed to identify cells. Cell z-stacks were color coded (*red: z1-25, green: z26- 50, blue: z51-75, gray: z76-100*) to distinguish different sections of the spheroid (**scale bar=100µm**). Mosaic images (overlay) of the color-coded sections highlight packing density of spheroids, which is increased for spheroids co-cultured with senescent MSCs.

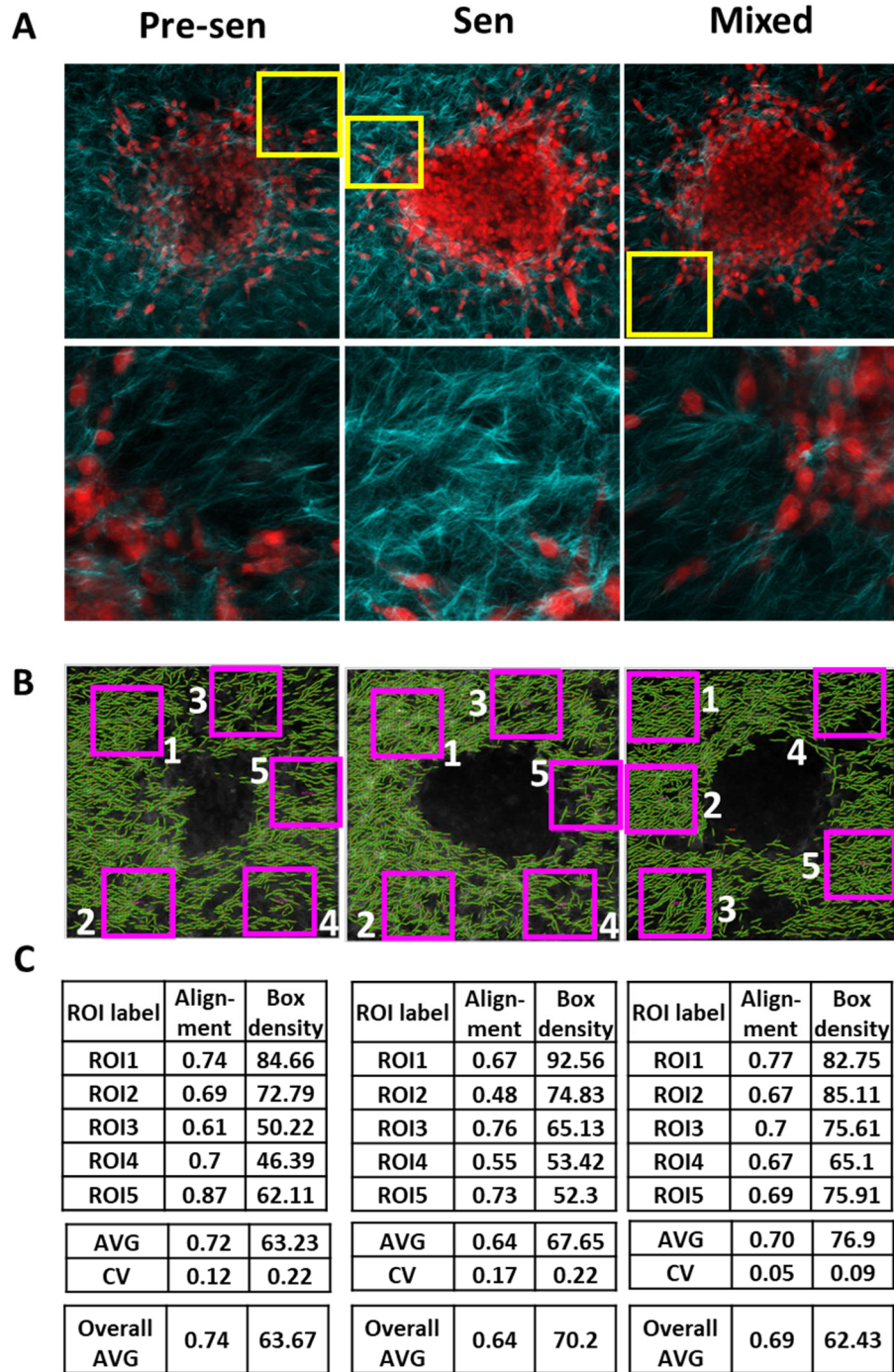


Figure S6. Analysis of local and global structure surrounding spheroids using CT-FIRE. (A) Spheroids embedded in collagen gels were imaged by multiphoton microscopy using second harmonic generation to identify collagen (shown in **cyan**) and NucRed to identify cells (shown in **red**); images include average intensity projections of z-stack and 2D slice for region highlighted by yellow box. (B-C) The structure of collagen around the embedded spheroid was analyzed using CurveAlign ROI analysis. For each image, 5 rectangular boxes were selected around the primary spheroid to quantify co-efficient of alignment. Properties of the ROIs along with the overall image are reported here.

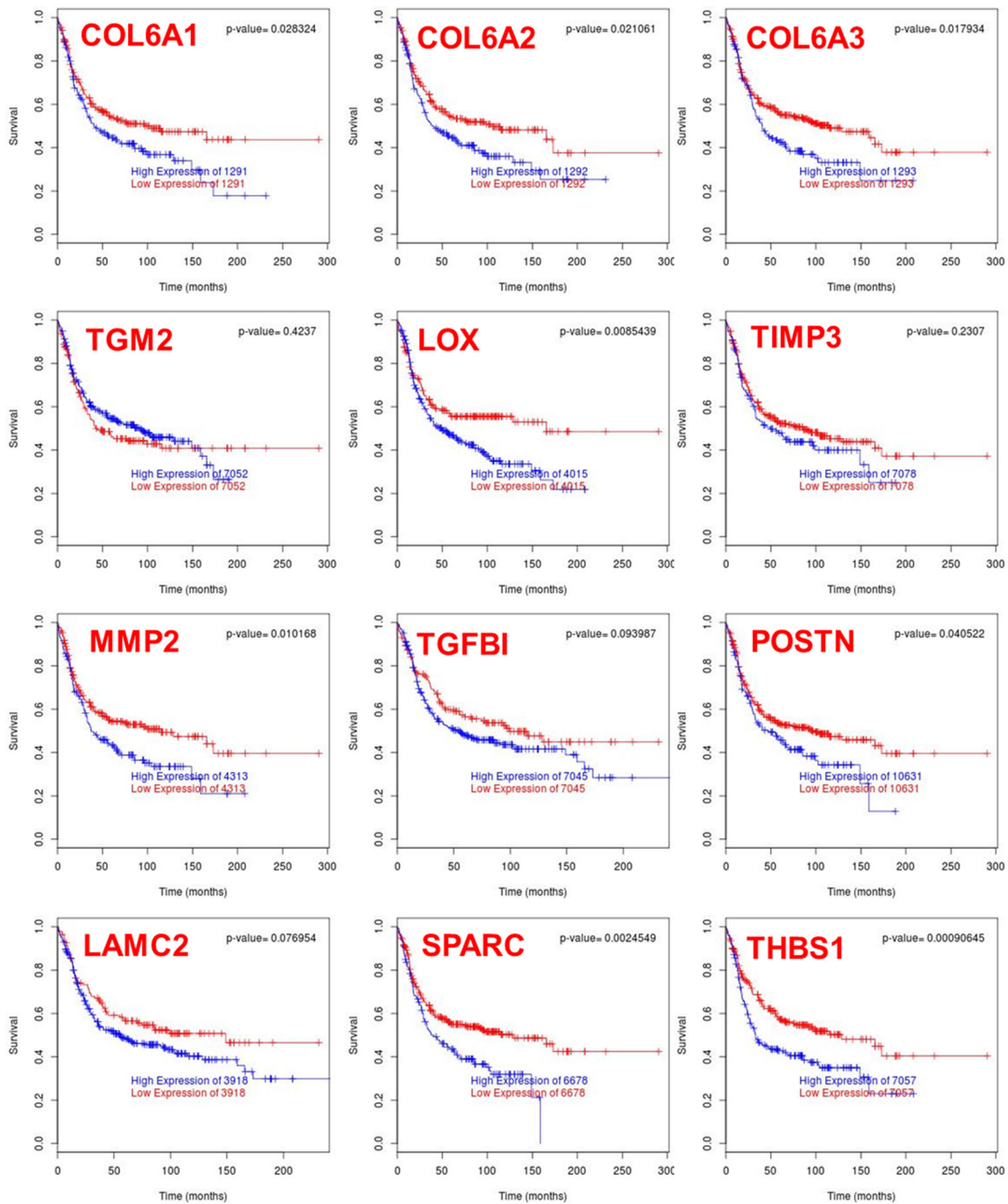


Figure S7. Survival analysis of senescent associated ECM signature in breast cancer. ECM signature from senescent MSCs was used to analyze Kaplan-Meier estimates of disease-free survival for breast cancer using free online tool BreastMark at <http://glados.ucd.ie/BreastMark/index.html>. ECM genes upregulated in senescent MSCs including, expression of collagen isoforms (COL6A1, COL6A2, COL6A3), matrix modifying enzymes (LOX, MMP2), and matricellular proteins (POSTN, THBS1, SPARC) are correlated with poor prognosis in basal subtype of breast cancer ($p < 0.05$).